reaction buffer for 16 h at 4 °C. Then, the linker-conjugated EGF and VP1-CMNPs were mixed at 1.15–1 weight ratio and were incubated for 12 h at 4 °C. After incubation, to quench the reaction, NaOH was added to the sample at a final concentration of 15 mM. The sample was mounted onto the top of 30% sucrose containing PBS and centrifuged at 230,000 × *g* for 15 min at 4 °C in a Beckman SW55Ti rotor. The pellet fraction containing EGF-conjugated $VP1^{WT}$-CMNPs or $VP1^{N138C}$-CMNPs was resuspended in PBS.

2.8. Cell binding assay

The human epidermoid carcinoma cell line, A431 (Hirabayashi et al., 1999) and the human colon adenocarcinoma cell line, WiDr (Noguchi et al., 1979) were kindly provided by Dr. M. Ueda (Keio University, Tokyo, Japan). A431 or WiDr cells (4×10^5 cells) were incubated with EGF-conjugated $VP1^{WT}$-CMNPs or $VP1^{N138C}$-CMNPs at an amount equivalent to 2 μg of VP1 in the presence or absence of various amounts of free EGF for 1 h at 4 °C in serum-free media. Free EGF was used to compete with EGF-conjugated nanoparticles for binding to the EGFR on the cell surface. Cells were collected, resuspended in SDS loading buffer, and then sonicated. Samples were separated by 10% SDS-PAGE, and Western analysis was performed with anti-VP1 (Ishizu et al., 2001) and anti-actin antibodies. Alternatively, sonicated samples were incubated with 100 μL of 6 N HCl for 30 min at 55 °C, and were then subjected to ICP-OES analyzer, Prodigy ICP (Teledyne Leeman Labs Inc, NH) to measure the Fe^{2+} concentration using yttrium as a standard.

3. Results and discussion

3.1. Synthesis of CMNPs coated with VP1

We have previously reported on the synthesis of water-dispersible CMNPs for use as an MRI contrast agent (Hatakeyama et al., 2011). For use *in vivo*, CMNPs should exhibit stable dispersibility in body fluid. To give the CMNPs an ability of active targeting to cells, here we aimed to synthesize CMNPs encapsulated with SV40-VLPs of 45 nm in diameter. As SV40-VLPs are dispersible *in vivo* and their surfaces can be easily modified by genetic or chemical methods, it led us to expect that encapsulation of CMNPs with SV40-VLPs would also be suitable for active targeting. To evaluate whether the CMNPs were encapsulated in SV40-VLPs, we used CMNPs with diameters of 8, 20, and 27 nm. Firstly, the CMNPs were mixed with wild-type VP1-pentamers ($VP1^{WT}$-pentamers) (the basic subunit of SV40-VLP) in a reaction buffer solution, and the mixtures were then dialyzed against a physiological buffer. Transmission electron microscope (TEM) measurements showed that all of the different-sized CMNPs mixed with $VP1^{WT}$-pentamers were covered with lightly stained layers of 5 nm in thickness (Fig. 1b, lower panels), compared to untreated CMNPs (Fig. 1b, upper panels). These results showed that $VP1^{WT}$-pentamer did not assemble into the 45-nm SV40-VLPs but coated CMNPs with a monolayer of $VP1^{WT}$-pentamer in a CMNP's size-dependent manner. Thus, coating of CMNPs with the $VP1^{WT}$-pentamer occurred instead of encapsulating CMNPs in VLPs. CMNPs coated with $VP1^{WT}$ ($VP1^{WT}$-CMNPs) were monodispersed under physiological salt conditions (Fig. 1b, lower panels), whereas control CMNPs formed aggregates in this buffer (Fig. 1b, upper panels). To further examine the dispersibility of CMNPs, we measured the size distribution of the particles in solution using dynamic light scattering (DLS). The average sizes of $VP1^{WT}$-CMNPs were approximately 10 nm larger than the diameters of original CMNPs (Fig. 1c), confirming that CMNPs of any given size could be coated with $VP1^{WT}$-pentamers. In contrast, the sizes of the control CMNPs in solution were roughly 500 nm, showing uncoated CMNPs to aggregation. Taken together, these findings demonstrated that VP1 coating yielded monodisperse CMNPs under physiological salt conditions.

Table 1
Relaxivities for different sized CMNPs with and without VP1-coating.

Core diameter	8 nm		20 nm		27 nm	
Coating	(−)	VP1	(−)	VP1	(−)	VP1
r_1 (s^{-1} mM^{-1})	30.1	14.8	29.8	16.5	34.3	20.4
r_2 (s^{-1} mM^{-1})	54.7	71.3	268.1	294.3	317.0	238.0
r_2/r_1	1.8	4.8	9.0	17.8	9.2	11.7

To directly examine whether the VP1 coating affected the surface properties of CMNPs, we measured the electric potential of their surfaces (Fig. 1d). Due to the citrate-coating, the surfaces of CMNPs were strongly charged with −18 mV at pH 7. In contrast, the surfaces of $VP1^{WT}$-CMNPs had a weak negative charge of −4 mV, indicating that VP1 coating changed the surface potential of CMNPs. Notably, this finding was supported by experiments showing that the surface potential of VLPs was comparable to that of $VP1^{WT}$-CMNPs.

To characterize the properties of VP1-CMNP as an MRI contrast agent, we measured the relaxivities (r_1, r_2) for different sized (8, 20 and 27 nm) CMNPs with and without VP1-coating in distilled water. The relaxivities of these VP1-CMNPs or CMNPs are shown in Table 1. Generally, at 0.47-T VP1-coating decreased the r_1 of the CMNPs without drastically affecting r_2. The subsequent increase in the r_2/r_1 ratio enhanced the potential of VP1-coated CMNPs as a T2 contrast agent. The r_1 for the 27 nm VP1-CMNPs was similar to that for conventional MRI contrast agents (ferucarbotran, Resovist™, $r_1 = 24.7\ s^{-1}\ mM^{-1}$) and the r_2 was large compared to that of ferucarbotran ($r_2 = 160.0\ s^{-1}\ mM^{-1}$). We also acquired T1- and T2-weighted MR images of 27 nm VP1-CMNPs at 7-T MRI with Gd-DTPA (gadopentetate dimeglumine, Magnevist™) and ferucarbotran (Fig. 1e). The signal intensity for VP1-CMNP in both the T1- and T2-weighted images gradually decreased with the VP1-CMNP concentration. The signal reduction for the VP1-CMNPs was larger than that for ferucarbotran on both T1- and T2-weighted images. From these results it is possible to speculate that VP1-CMNPs have better capability as a T2 contrast agent than conventional ferucarbotran.

The C-terminal region of VP1 is important for pentamer–pentamer interaction between VP1-pentamers during the assembly of SV40-VLPs (Garcea et al., 1987; Yokoyama et al., 2007). Using a VP1 mutant with a 58 amino-acid deletion in the C-terminal region ($VP1^{\Delta C58}$), we investigated whether the pentamer–pentamer interaction would be required for the VP1 coating on the surface of CMNPs. CMNPs were mixed with either $VP1^{WT}$-pentamers or $VP1^{\Delta C58}$-pentamers, and were then examined under the TEM. As shown in Fig. 2a, lightly stained layers 5 nm-thick were around CMNPs regardless of whether the $VP1^{WT}$ or the $VP1^{\Delta C58}$ was used, suggesting that the pentamer–pentamer interaction was not necessary for the attachment of VP1-pentamers onto the surfaces of CMNPs. Unlike $VP1^{WT}$-CMNPs (Fig. 2a, left panel), however, $VP1^{\Delta C58}$-attached CMNPs formed particulate aggregates in physiological buffer solution (Fig. 2a, right panel). We have previously reported that DNA is coated with $VP1^{WT}$-pentamers and therefore promotes the assembly of $VP1^{WT}$-pentamers into 45 nm spherical particles (Tsukamoto et al., 2007). Time-course analysis of this DNA-mediated assembly suggests that $VP1^{WT}$-pentamers form aggregates within the first 1 h of reaction, and then form spherical particles through the interaction between $VP1^{WT}$-pentamers in the next 1 h (Tsukamoto et al., 2007). From this point of view, $VP1^{\Delta C58}$-attached CMNPs lacking the pentamer–pentamer interaction may correspond to $VP1^{WT}$-attached DNA in the early stages of the reaction. To examine the dispersibility of $VP1^{\Delta C58}$-attatched CMNPs under physiological

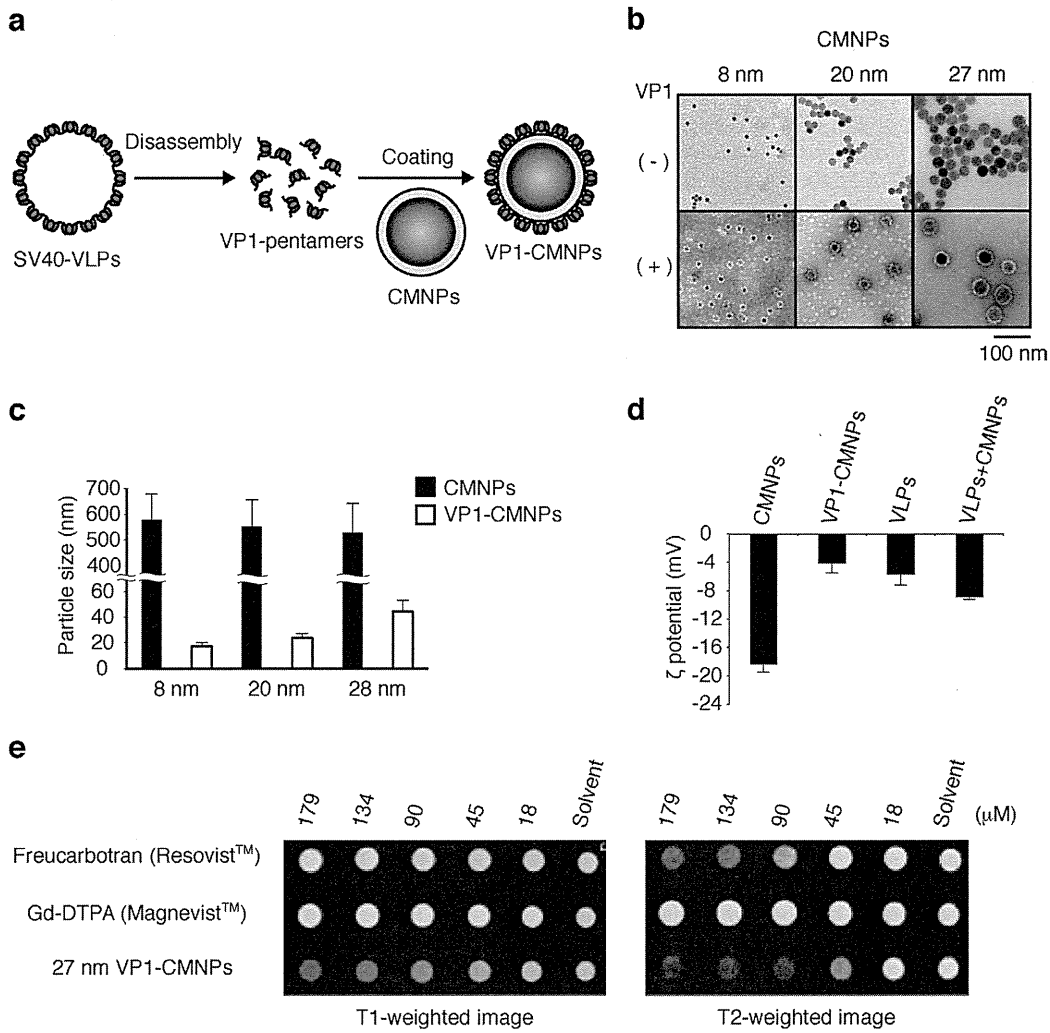

Fig. 1. Synthesis and characterization of VP1-CMNPs. (a) Schematic diagram of the construction of VP1-CMNPs. SV40-VLPs were dissociated into VP1-pentamers. The surfaces of CMNPs were then coated with VP1-pentamers (VP1-CMNPs). (b) Three different-sized CMNPs of 8, 20, and 27 nm in diameter were incubated with (+) or without (−) $VP1^{WT}$-pentamers during dialysis. The samples were visualized by negative staining under the TEM. Scale bar: 100 nm. (c) Diameters of intact CMNPs (black bars) and $VP1^{WT}$-CMNPs (white bars) in the physiological buffer were measured by DSL. Data are shown as the mean ± SD. (d) Zeta-potential of intact CMNPs, $VP1^{WT}$-CMNPs, or SV40-VLPs was analyzed. Data are shown as the mean ± SD. (e) T1-weighted (left) and T2-weighted (right) MR images of MNP (Upper, Ferucarbotran, resovist™), Gd-DTPA and 27 nm VP1-CMNPs at various concentrations. Samples of distilled water were measured as references.

conditions, we carried out sucrose gradient sedimentation analysis (Fig. 2b) (Kawano et al., 2006). After centrifugation, 12 fractions were collected from the top of the gradient. $VP1^{WT}$-CMNPs were found in fractions 5–9 (Fig. 2b, upper panel), whereas $VP1^{\Delta C58}$-attatched CMNPs were detected in the bottom fraction (Fig. 2b, lower panel), suggesting the aggregation of the nanoparticles. These results imply that the pentamer–pentamer interaction is required for the formation of dispersible $VP1^{WT}$-CMNPs.

3.2. Dispersibility of VP1-CMNPs in serum

Practical applications of diagnosis necessitate their dispersibility in body fluids. Therefore, we examined the degree to which $VP1^{WT}$-CMNPs would disperse in serum. $VP1^{WT}$-CMNPs and control CMNPs were incubated in either phosphate buffered saline (PBS) or fetal bovine serum (FBS). In agreement with the data in Fig. 1b and c, $VP1^{WT}$-CMNPs were highly dispersible in PBS, while the control CMNPs aggregated together (Fig. 3a). Surprisingly, $VP1^{WT}$-CMNPs were still dispersible even in FBS (Fig. 3a) although intact CMNPs formed aggregates (Fig. 3a). To verify the TEM results, we measured the diameter of CMNPs. DLS analysis showed that the diameter of $VP1^{WT}$-CMNPs was approximately 40 nm in both PBS and FBS (Fig. 3b), indicating that $VP1^{WT}$-CMNPs were monodispersed in FBS as well as PBS. On the other hand, the control CMNPs in PBS and FBS were 400 and 150 nm in diameter, respectively (Fig. 3b), showing that the water-dispersible, control CMNPs did not disperse in either PBS or FBS. To verify the dispersibility of $VP1^{WT}$-CMNPs *in vivo*, mice were administrated intravenously with an equal dose of CMNPs or $VP1^{WT}$-CMNPs, and the concentration of CMNPs-derived Fe^{2+} in the blood was measured at various times. We expected that highly dispersible $VP1^{WT}$-CMNPs would keep drifting in the blood stream, whereas aggregated CMNPs would tend to settle down and to be quickly uptaken in the liver. As shown in Fig. 3c, the basal Fe^{2+} concentration in both cases was approximately 0.5 mg/μL just before injection. Moreover, we observed rapid increases in Fe^{2+} concentration in both cases just after injection. However, the Fe^{2+} concentration in $VP1^{WT}$-CMNPs-injected mice was approximately twice of that in CMNPs-injected mice at this point in time (Fig. 3c). Furthermore, the Fe^{2+} concentration in both cases gradually decreased to basal level. In addition, the Fe^{2+} concentration decreased much slower in $VP1^{WT}$-CMNPs-injected mice (a half-life of 45 min) than in CMNPs-injected mice (a half-life

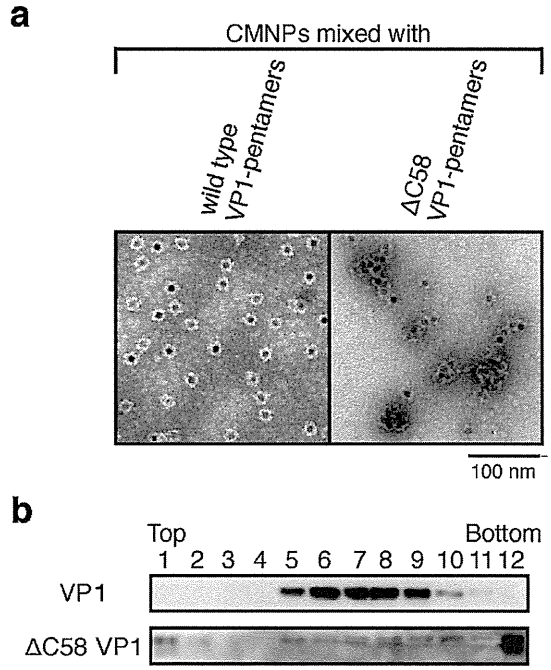

Fig. 2. Requirements of the pentamer–pentamer interaction in the VP1 coating. (a) $VP1^{WT}$-CMNPs (left panel) and $VP1^{\Delta C58}$-CMNPs (right panel) of 8 nm in diameter were observed under the TEM. Scale bar: 100 nm. (b) Sucrose gradient sedimentation analyses of $VP1^{WT}$-CMNPs (upper panel) and $VP1^{\Delta C58}$-CMNP (lower panel) of 8 nm in diameter were performed. Fractions were separated by 10% SDS-PAGE and analyzed by Western blot with anti-VP1 antibody. Fractions were numbered from the top to the bottom of the gradient.

of 45 s; Fig. 3c), indicating the longer retention time of $VP1^{WT}$-CMNPs in blood. These results strongly suggest that $VP1^{WT}$-CMNPs are dispersive *in vivo*. In this study, the profound liver uptake of aggregated CMNPs might induce quick decline of CMNPs-derived Fe^{2+} concentration in the blood.

3.3. Targeting of EGFR-overexpressing tumor cells by EGF-conjugated VP1-CMNPs

Because EGFR is overexpressed on the surface of various tumor cells (Normanno et al., 2003; Salomon et al., 1995), it is possible to target certain tumor cells through EGFR. We previously constructed SV40-VLPs conjugated with EGF using the heterobifunctional crosslinker, $SM(PEG)_2$ and $VP1^{N138C}$, in which an asparagine (N) residue located on the outside surface of VLPs (Takahashi et al., 2008) was substituted to a cysteine (C) residue (Kitai et al., 2011). The EGF-conjugated SV40-VLPs were shown to selectively target EGFR-expressing tumor cells *in vitro* (Kitai et al., 2011). Since $SM(PEG)_2$ preferably crosslinks between a primary amine of EGF and the cysteine residue of $VLPs^{N138C}$, EGF is considered to be selectively attached to the outside surface of $VLPs^{N138C}$. Moreover, although $VP1^{WT}$ has a partially accessible cysteine residue on the surface of VP1-pentamer, $VP1^{N138C}$ has additional cysteine residue on the surface loop of VP1. It leads us to expect that EGF might be more functionally present on the surface of $VP1^{N138C}$ than $VP1^{WT}$. In addition, $VLPs^{WT}$ generally bind to a variety of cells through the interaction between the BC, DE, and HI loops of VP1 and GM1 ganglioside on the cells (Takahashi et al., 2008). However, the mutation at position 138 elicits the conformational change of DE loop, and thereby disrupts the binding of EGF-conjugated $VLPs^{N138C}$ to various cells without EGFR expression. Consequently, EGF-conjugated $VLPs^{N138C}$ may be engaged exclusively in EGF-specific targeting.

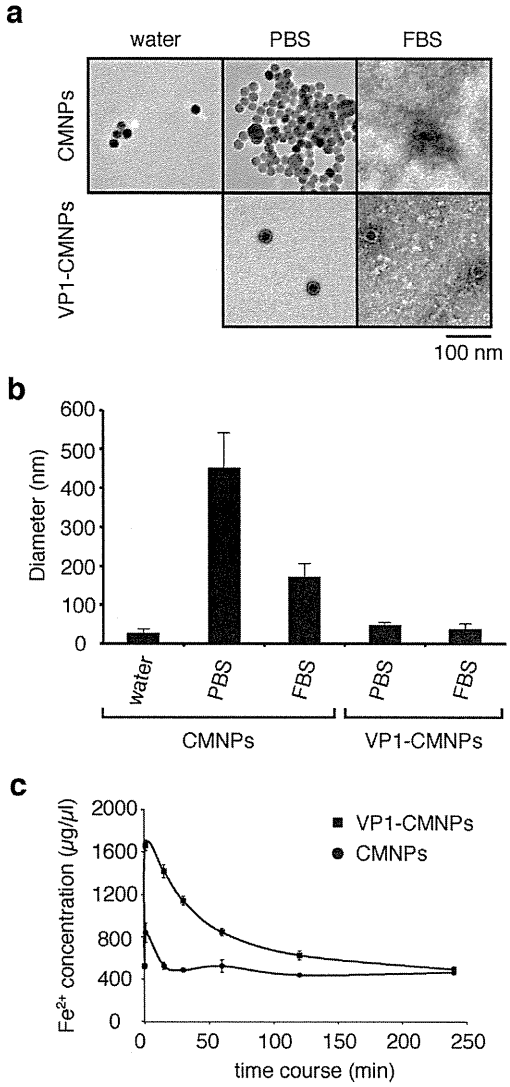

Fig. 3. Dispersibility of VP1-CMNPs *in vitro* and *in vivo*. (a) Intact CMNPs (upper panels) and $VP1^{WT}$-CMNPs (lower panels) of 27 nm in diameter were incubated in water (left panel), PBS (center panels), or FBS (right panels), and were observed under the TEM. Scale bar: 100 nm. (b) Diameters of intact CMNPs and $VP1^{WT}$-CMNPs in water, PBS, or FBS were analyzed by DLS. (c) BALB/c mice were injected intravenously with either intact CMNPs or $VP1^{WT}$-CMNPs of 27 nm in diameter. Blood was collected from each mouse at various time points after injection, and the concentration of Fe^{2+} in the blood was measured by ICP-OES analyzer. Data are shown as the mean ± SD of three samples.

Based on these data (Kitai et al., 2011) and ideas, $VP1^{N138C}$-coated 27-nm CMNPs ($VP1^{N138C}$-CMNPs) were synthesized, and EGF conjugated to both $VP1^{WT}$-CMNPs and $VP1^{N138C}$-CMNPs using the crosslinker (Fig. 4a). By calculating the intensity of the protein bands from Fig. 4b, the percentage of EGF conjugated to $VP1^{N138}$ protein in total $VP1^{N138}$ protein of $VP1^{N138C}$-CMNPs appeared to be 26% only slightly larger than that of 18% in $VP1^{WT}$-CMNPs, suggesting that $VP1^{N138C}$ presents more functionally EGF than $VP1^{WT}$. $VP1^{N138C}$-CMNPs were found to be monodispersed in physiological buffer regardless of EGF conjugation (Fig. 4c).

To assess the specificity and efficiency of tumor-targeting by EGF-conjugated $VP1^{N138C}$-CMNPs, we performed cell binding assay using two human tumor cell lines, A431 (Hirabayashi et al., 1999) and WiDr (Noguchi et al., 1979), which express high and low levels of EGFR, respectively. $VP1^{WT}$-CMNPs and $VP1^{N138C}$-CMNPs conjugated with or without EGF were incubated with either A431

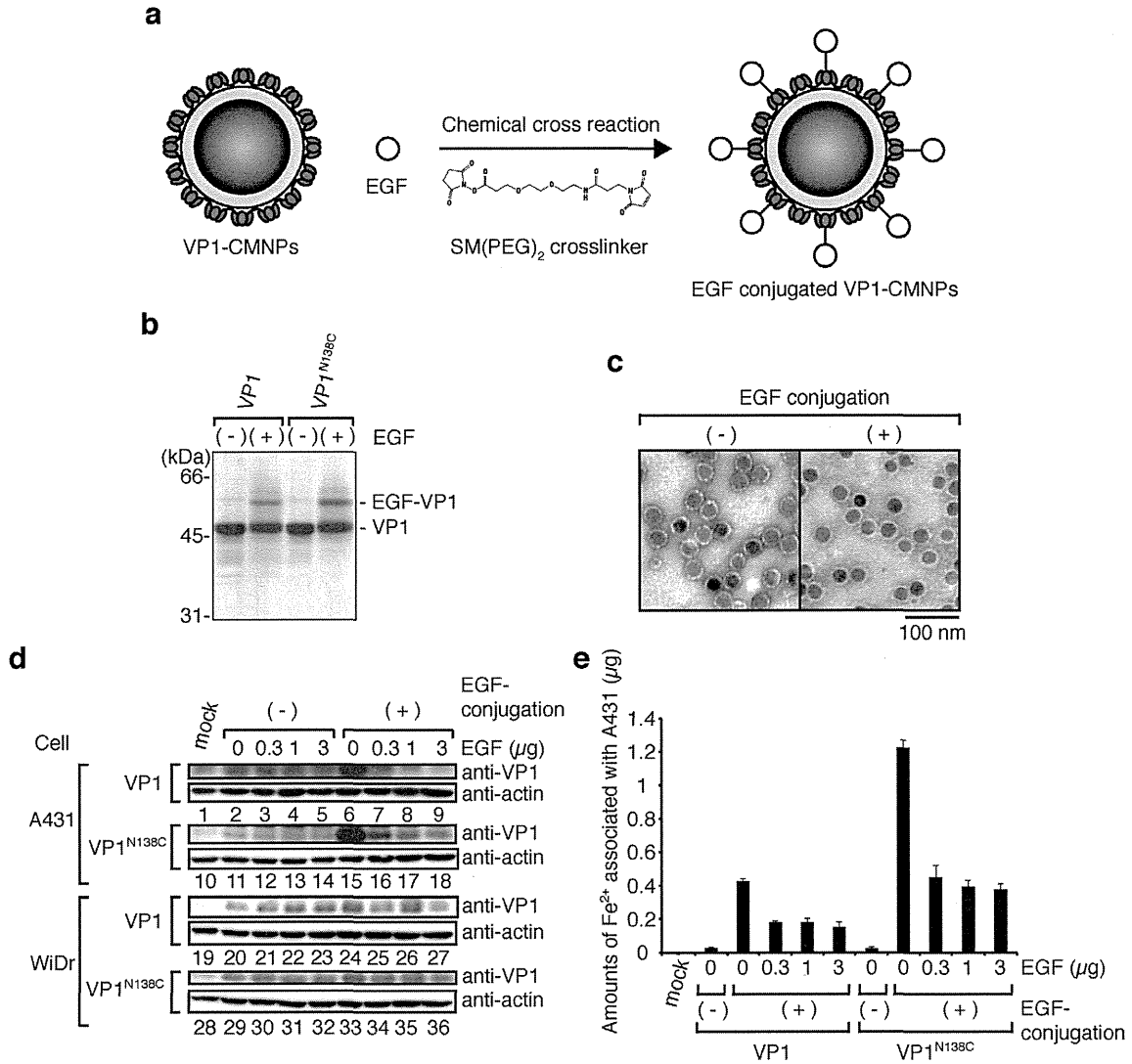

Fig. 4. Targeting of EGFR-overexpressing tumor cells by EGF-conjugated VP1-CMNPs. (a) Schematic diagram of EGF conjugation. EGF was conjugated onto the surface of VP1-CMNPs of 27 nm in diameter using $SM(PEG)_2$ crosslinker. (b) $VP1^{WT}$-CMNPs and $VP1^{N138C}$-CMNPs with (+) or without (-) EGF were loaded onto 10% SDS-PAGE. Positions of EGF conjugated VP1 and free VP1 were indicated. (c) TEM imaging of unconjugated-$VP1^{N138C}$-CMNPs (left panel) and EGF-conjugated $VP1^{N138C}$-CMNPs (right panel). Scale bar: 100 nm. (d) and (e) Cell binding assay. A431 or WiDr cells were incubated with EGF-conjugated either $VP1^{WT}$-CMNPs or $VP1^{N138C}$-CMNPs in the presence or absence of various amounts of free EGF. After incubation, cell lysate were separated by 10% SDS-PAGE, and analyzed by Western blot with anti-VP1 and anti-actin antibodies (d). Alternatively, samples were subjected to ICP-OES analysis to measure the concentration of Fe^{2+} (e). Data are shown as the mean ± SD of triplicate samples.

or WiDr cells in the presence or absence of various concentrations of free EGF. Cells were then subjected to immunoblotting using anti-VP1 antibody. As shown in Fig. 4d, both EGF-conjugated $VP1^{WT}$- and $VP1^{N138C}$-CMNPs much more associated with A431 cells than those of EGF-unconjugated, whereas the associations of WiDr cells with $VP1^{WT}$- and $VP1^{N138C}$-CMNPs were comparable regardless of EGF conjugation. The association of A431 cells with EGF-conjugated $VP1^{N138C}$-CMNPs was significantly inhibited by the addition of 0.3 μg free EGF and competition was saturated (Fig. 4d, lanes 15–18). A similar inhibition pattern was observed in the association between A431 cells and EGF-conjugated $VP1^{WT}$-CMNPs (Fig. 4d, lanes 6–9). On the other hand, the association of WiDr cells with either EGF-conjugated $VP1^{WT}$-CMNPs or $VP1^{N138C}$-CMNPs was hardly detected in this assay (Fig. 4d, lanes 24–27 and 33–36). These results indicate that EGF-conjugated $VP1^{N138C}$-CMNPs and $VP1^{WT}$-CMNPs specifically attach to tumor cells through the EGF-EGFR interaction. It is noteworthy that the amounts of $VP1^{N138C}$-CMNPs attached to A431 cells (lane 15) were significantly larger than those of $VP1^{WT}$-CMNPs (lanes 6), suggesting that the $VP1^{N138C}$-CMNPs target EGFR-expressing tumor cells more effectively than the $VP1^{WT}$-CMNPs.

To further evaluate the selective association, we analyzed the amount of CMNPs-derived Fe^{2+} with A431 cells using the inductively coupled plasma optical emission spectrometry (ICP-OES) analyzer (Prodigy ICP). As shown in Fig. 4e, the conjugation of EGF to $VP1^{WT}$-CMNPs and $VP1^{N138C}$-CMNPs dramatically increased the amounts of Fe^{2+} associated with A431 cells. Consistent with the data in Fig. 4d, quantification of Fe^{2+} indicated that the amount of EGF-conjugated $VP1^{N138C}$-CMNPs bound to A431 cells was 3-fold larger than that of EGF-conjugated $VP1^{WT}$-CMNPs (Fig. 4e). Moreover, the addition of 0.3 μg free EGF to this system lowered the cell-associated levels of Fe^{2+} for both $VP1^{WT}$-CMNPs and $VP1^{N138C}$-CMNPs and the competition was saturated at this concentration. Remained Fe^{2+} amounts associated with A431 cells in the range of 1 and 3 μg free EGF concentration might be due to the EGFR-nonspecific binding of $VP1^{WT}$-CMNPs and $VP1^{N138C}$-CMNPs. Taken

together, these data demonstrate that $VP1^{N138C}$-CMNPs are able to present EGF more effectively than $VP1^{WT}$-CMNPs so that the particles are targeted to EGFR-expressing tumor cells with remarkable specificity *in vitro*.

4. Conclusions

We showed that VP1 coating allows CMNPs to be monodispersed in body fluid such as serum and blood (Fig. 3a–c). This characteristic is very important for MRI contrast agents because monodispersible nanoparticles can reach tissues or organs by traveling in the blood stream. Since it has been suggested that viral capsid protein is a suitable material to achieve biocompatibility (Cormode et al., 2010), the VP1 coating may be also expected to provide biocompatibility to the nanoparticle and prevent their detection and elimination by the clearance mechanisms in the body. In addition, VP1 based architecture is shown to be very stable in broad range of salt concentration, pH, and temperature (Kawano et al., 2009) and considered to be safe for humans to use them as a vaccine material because there is no evidence that SV40 VP1 protein has acute or chronic cytotoxicity against human cells (Hilleman, 1998; Butel and Lednicky, 1999). Moreover, the VP1 coating allows further modification on the surface of CMNPs. As previously described (Bulte et al., 1994; Uchida et al., 2006), our results support that protein cages such as viral capsids or ferritins are promising platform for diagnosis use.

The most desirable feature of agents for diagnosis is the ability to target intended tissues or tumors *in vivo*. The distribution of nanoparticles in the body is affected by multiple factors such as molecular size, shape and charge (Longmire et al., 2008). For instance, certain sizes of nanoparticles tend to be accumulated in tumor tissues through enhanced permeability and retention (Maeda et al., 2000), which is known as the enhanced permeability and retention (EPR) effect (Maeda, 2001). Apart from such passive targeting, active delivery and retention of nanoparticles into tissues or tumors is still far from reality although much effort has been devoted to designing probes that detect tumors. However, active targeting is of great interest to many clinicians because this technique will allow accurate diagnosis of tumor at an early stage. Tumor-specific monoclonal antibodies may be the ultimate tool for the active targeting. A number of investigators have studied this issue using small animals (Anderson et al., 2000; Gohr-Rosenthal et al., 1993; Remsen et al., 1996; Shahbazi-Gahrouei et al., 2001; Sipkins et al., 1998; Suwa et al., 1998). However, considering the large amount of antibody used, this approach may be too costly for commercial use (Weinmann et al., 2003). On the other hand, it has been suggested that EGFR represents an ideal target for diagnosis and therapy of human carcinomas (Normanno et al., 2003; Salomon et al., 1995; Suwa et al., 1998). A majority of human solid tumors overexpress high levels of EGFR, and the overexpression level is often correlated with a poor prognosis (Salomon et al., 1995).

Because tumor cells are more heat-sensitive than normal cells, hyperthermia has served as an anti-tumor therapy (Falk and Issels, 2001; Koga et al., 1983; van der Zee, 2002). Since MNPs can be used for hyperthermia as a heater element (Gupta and Gupta, 2005), EGF-conjugated $VP1^{N138C}$-CMNPs may be directly applicable to tumor-targeted hyperthermia therapy. That is, EGF-immobilized $VP1^{N138C}$-CMNPs has a great potential for an excellent therapeutic material as well as a diagnostic material.

Acknowledgments

This work was supported by Special Coordination Funds for Promoting Science and Technology from JST, by the Global COE (Center of Excellence) Program from the Japan Ministry of Education, Culture, Sports, Science, and Technology (MEXT), and by a grant for Research and Development Projects in Cooperation with Academic Institutions from the New Energy and Technology Development Organization (to H.H.). This work was also supported by Grant-in-Aid for Scientific Research (A) (21241019 to H.H.) from MEXT.

The authors are grateful to Dr. M. Ueda (Keio University) and K. Doi, H. Kishi, K. Imai, and S. Nomura (Tokyo Institute of Technology) for providing A431 and WiDr cell lines and for the assistance of material preparation, respectively.

References

Anderson, S.A., Rader, R.K., Westlin, W.F., Null, C., Jackson, D., Lanza, G.M., Wickline, S.A., Kotyk, J.J., 2000. Magnetic resonance contrast enhancement of neovasculature with alpha(v)beta(3)-targeted nanoparticles. Magnetic Resonance in Medicine 44, 433–439.

Bulte, J.W., Douglas, T., Mann, S., Frankel, R.B., Moskowitz, B.M., Brooks, R.A., Baumgarner, C.D., Vymazal, J., Strub, M.P., Frank, J.A., 1994. Magnetoferritin: characterization of a novel superparamagnetic MR contrast agent. Journal of Magnetic Resonance Imaging 4, 497–505.

Butel, J.S., Lednicky, J.A., 1999. Cell and molecular biology of simian virus 40: implications for human infections and disease. Journal of the National Cancer Institute 91, 119–134.

Cormode, D.P., Jarzyna, P.A., Mulder, W.J., Fayad, Z.A., 2010. Modified natural nanoparticles as contrast agents for mediccal imaging. Adv. Drug Deliv. Rev. 62, 329–338.

Enomoto, T., Kukimoto, I., Kawano, M.A., Yamaguchi, Y., Berk, A.J., Handa, H., 2011. In vitro reconstitution of SV40 particles that are composed of VP1/2/3 capsid proteins and nucleosomal DNA and direct efficient gene transfer. Virology 420, 1–9.

Falk, M.H., Issels, R.D., 2001. Hyperthermia in oncology. International Journal of Hyperthermia 17, 1–18.

Garcea, R.L., Salunke, D.M., Caspar, D.L., 1987. Site-directed mutation affecting polyomavirus capsid self-assembly *in vitro*. Nature 329, 86–87.

Gohr-Rosenthal, S., Schmitt-Willich, H., Ebert, W., Conrad, J., 1993. The demonstration of human tumors on nude mice using gadolinium-labelled monoclonal antibodies for magnetic resonance imaging. Investigative Radiology 28, 789–795.

Gupta, A.K., Gupta, M., 2005. Synthesis and surface engineering of iron oxide nanoparticles for biomedical applications. Biomaterials 26, 3995–4021.

Hatakeyama, M., Kishi, H., Kita, Y., Imai, K., Nishio, K., Karasawa, S., Masaike, Y., Sakamoto, S., Sandhu, A., Tanimoto, A., Gomi, T., Kohda, E., Abe, M., Handa, H., 2011. A two-step ligand exchange reaction generates highly water-dispersed magnetic nanoparticles for biomedical applications. Journal of Materials Chemistry 21, 5959–5966.

Hilleman, M.R., 1998. Discovery of simian virus 40 (SV40) and its relationship to poliomyelitis virus vaccines. Developments in Biological Standardization 94, 183–190.

Hirabayashi, K., Yano, J., Inoue, T., Yamaguchi, T., Tanigawara, K., Smyth, G.E., Ishiyama, K., Ohgi, T., Kimura, K., Irimura, T., 1999. Inhibition of cancer cell growth by polyinosinic–polycytidylic acid/cationic liposome complex: a new biological activity. Cancer Research 59, 4325–4333.

Inoue, T., Kawano, M.A., Takahashi, R.U., Tsukamoto, H., Enomoto, T., Imai, T., Kataoka, K., Handa, H., 2008. Engineering of SV40-based nano-capsules for delivery of heterologous proteins as fusions with the minor capsid proteins VP2/3. Journal of Biotechnology 134, 181–192.

Ishizu, K.I., Watanabe, H., Han, S.I., Kanesashi, S.N., Hoque, M., Yajima, H., Kataoka, K., Handa, H., 2001. Roles of disulfide linkage and calcium ion-mediated interactions in assembly and disassembly of virus-like particles composed of simian virus 40 VP1 capsid protein. Journal of Virology 75, 61–72.

Kanesashi, S.N., Ishizu, K., Kawano, M.A., Han, S.I., Tomita, S., Watanabe, H., Kataoka, K., Handa, H., 2003. Simian virus 40 VP1 capsid protein forms polymorphic assemblies *in vitro*. Journal of General Virology 84, 1899–1905.

Kawano, M.A., Inoue, T., Tsukamoto, H., Takaya, T., Enomoto, T., Takahashi, R.U., Yokoyama, N., Yamamoto, N., Nakanishi, A., Imai, T., Wada, T., Kataoka, K., Handa, H., 2006. The VP2/VP3 minor capsid protein of simian virus 40 promotes the *in vitro* assembly of the major capsid protein VP1 into particles. Journal of Biological Chemistry 281, 10164–10173.

Kawano, M.A., Xing, L., Tsukamoto, H., Inoue, T., Handa, H., Cheng, R.H., 2009. Calcium bridge triggers capsid disassembly in the cell entry process of simian virus 40. Journal of Biological Chemistry 284, 34703–34712.

Kitai, Y., Fukuda, H., Enomoto, T., Asakawa, Y., Suzuki, T., Inouye, S., Handa, H., 2011. Cell selective targeting of a simian virus 40 virus-like particle conjugated to epidermal growth factor. Journal of Biotechnology 155, 251–256.

Koga, S., Izumi, A., Maeta, M., Shimizu, N., Osaki, Y., Kanayama, H., 1983. The effects of total-body hyperthermia combined with anticancer drugs on immunity in advanced cancer patients. Cancer 52, 1173–1177.

Kosukegawa, A., Arisaka, F., Takayama, M., Yajima, H., Kaidow, A., Handa, H., 1996. Purification and characterization of virus-like particles and pentamers produced by the expression of SV40 capsid proteins in insect cells. Biochimica et Biophysica Acta 1290, 37–45.

Liddington, R.C., Yan, Y., Moulai, J., Sahli, R., Benjamin, T.L., Harrison, S.C., 1991. Structure of simian virus 40 at 3.8-A resolution. Nature 354, 278–284.

Longmire, M., Choyke, P.L., Kobayashi, H., 2008. Clearance properties of nano-sized particles and molecules as imaging agents: considerations and caveats. Nanomedicine (Lond) 3, 703–717.

Maeda, H., 2001. The enhanced permeability and retention (EPR) effect in tumor vasculature: the key role of tumor-selective macromolecular drug targeting. Advances in Enzyme Regulation 41, 189–207.

Maeda, H., Wu, J., Sawa, T., Matsumura, Y., Hori, K., 2000. Tumor vascular permeability and the EPR effect in macromolecular therapeutics: a review. Journal of Controlled Release 65, 271–284.

Montet, X., Montet-Abou, K., Reynolds, F., Weissleder, R., Josephson, L., 2006. Nanoparticle imaging of integrins on tumor cells. Neoplasia 8, 214–222.

Nasongkla, N., Bey, E., Ren, J., Ai, H., Khemtong, C., Guthi, J.S., Chin, S.F., Sherry, A.D., Boothman, D.A., Gao, J., 2006. Multifunctional polymeric micelles as cancer-targeted, MRI-ultrasensitive drug delivery systems. Nano Letters 6, 2427–2430.

Noguchi, P., Wallace, R., Johnson, J., Earley, E.M., O'Brien, S., Ferrone, S., Pellegrino, M.A., Milstien, J., Needy, C., Browne, W., Petricciani, J., 1979. Characterization of the WIDR: a human colon carcinoma cell line. In Vitro 15, 401–408.

Normanno, N., Maiello, M.R., De Luca, A., 2003. Epidermal growth factor receptor tyrosine kinase inhibitors (EGFR-TKIs): simple drugs with a complex mechanism of action? Journal of Cellular Physiology 194, 13–19.

Remsen, L.G., McCormick, C.I., Roman-Goldstein, S., Nilaver, G., Weissleder, R., Bogdanov, A., Hellstrom, I., Kroll, R.A., Neuwelt, E.A., 1996. MR of carcinoma-specific monoclonal antibody conjugated to monocrystalline iron oxide nanoparticles: the potential for noninvasive diagnosis. American Journal of Neuroradiology 17, 411–418.

Salomon, D.S., Brandt, R., Ciardiello, F., Normanno, N., 1995. Epidermal growth factor-related peptides and their receptors in human malignancies. Critical Reviews in Oncology/Hematology 19, 183–232.

Shahbazi-Gahrouei, D., Williams, M., Rizvi, S., Allen, B.J., 2001. In vivo studies of Gd-DTPA-monoclonal antibody and gd-porphyrins: potential magnetic resonance imaging contrast agents for melanoma. Journal of Magnetic Resonance Imaging 14, 169–174.

Sipkins, D.A., Cheresh, D.A., Kazemi, M.R., Nevin, L.M., Bednarski, M.D., Li, K.C., 1998. Detection of tumor angiogenesis *in vivo* by alphaVbeta3-targeted magnetic resonance imaging. Nature Medicine 4, 623–626.

Suwa, T., Ozawa, S., Ueda, M., Ando, N., Kitajima, M., 1998. Magnetic resonance imaging of esophageal squamous cell carcinoma using magnetite particles coated with anti-epidermal growth factor receptor antibody. International Journal of Cancer 75, 626–634.

Takahashi, R.U., Kanesashi, S.N., Inoue, T., Enomoto, T., Kawano, M.A., Tsukamoto, H., Takeshita, F., Imai, T., Ochiya, T., Kataoka, K., Yamaguchi, Y., Handa, H., 2008. Presentation of functional foreign peptides on the surface of SV40 virus-like particles. Journal of Biotechnology 135, 385–392.

Tsukamoto, H., Kawano, M.A., Inoue, T., Enomoto, T., Takahashi, R.U., Yokoyama, N., Yamamoto, N., Imai, T., Kataoka, K., Yamaguchi, Y., Handa, H., 2007. Evidence that SV40 VP1-DNA interactions contribute to the assembly of 40-nm spherical viral particles. Genes to Cells 12, 1267–1279.

Uchida, M., Flenniken, M.L., Allen, M., Willits, D.A., Crowley, B.E., Brumfield, S., Willis, A.F., Jackiw, L., Jutila, M., Young, M.J., Douglas, T., 2006. Targeting of cancer cells with ferrimagnetic ferritin cage nanoparticles. Journal of the American Chemical Society 128, 16626–16633.

van der Zee, J., 2002. Heating the patient: a promising approach? Annals of Oncology 13, 1173–1184.

Weinmann, H.J., Ebert, W., Misselwitz, B., Schmitt-Willich, H., 2003. Tissue-specific MR contrast agents. European Journal of Radiology 46, 33–44.

Yokoyama, N., Kawano, M.A., Tsukamoto, H., Enomoto, T., Inoue, T., Takahashi, R.U., Nakanishi, A., Imai, T., Wada, T., Handa, H., 2007. Mutational analysis of the carboxyl-terminal region of the SV40 major capsid protein VP1. Journal of Biochemistry 141, 279–286.

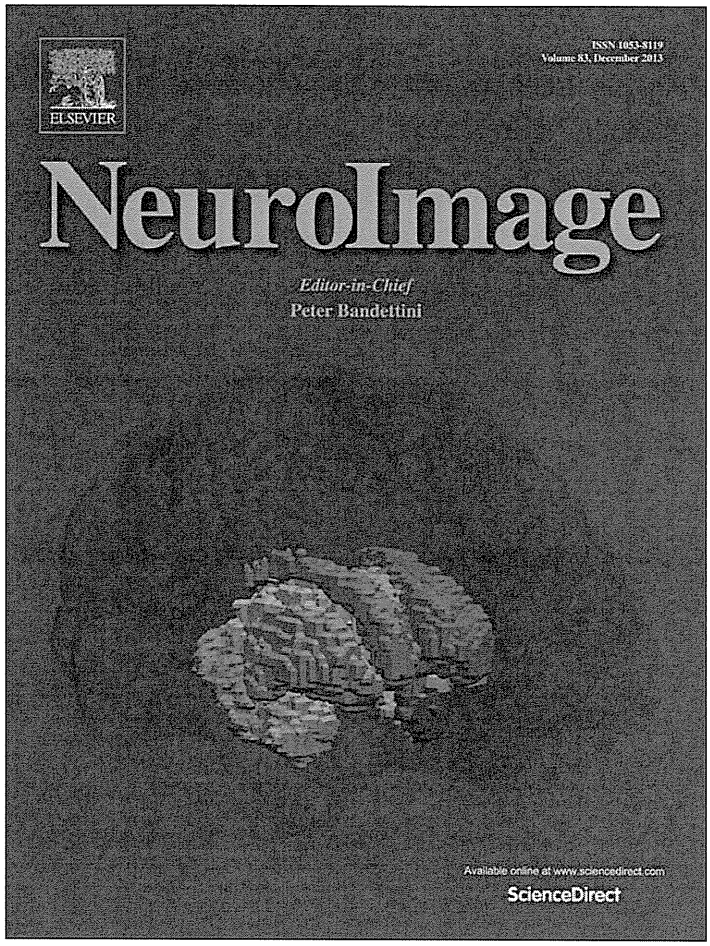

NeuroImage 83 (2013) 294–306

Contents lists available at ScienceDirect

NeuroImage

journal homepage: www.elsevier.com/locate/ynimg

MRI-based morphometric characterizations of sexual dimorphism of the cerebrum of ferrets (*Mustela putorius*)

Kazuhiko Sawada [a,*], Miwa Horiuchi-Hirose [b], Shigeyoshi Saito [c], Ichio Aoki [d]

[a] Department of Physical Therapy, Faculty of Medical and Health Sciences, Tsukuba International University, Tsuchiura, Ibaraki 300-0051, Japan
[b] Department of Nutrition, Faculty of Medical and Health Sciences, Tsukuba International University, Tsuchiura, Ibaraki 300-0051, Japan
[c] Department of Medical Engineering, Division of Health Sciences, Osaka University Graduate School of Medicine, Suita, Osaka 565-0871, Japan
[d] Molecular Imaging Center, National Institute of Radiological Sciences, Chiba 263-8555, Japan

ARTICLE INFO

Article history:
Accepted 3 June 2013
Available online 14 June 2013

Keywords:
Phylogeny
Evolution
Brain
Neurodevelopmental disorders
Sexual dimorphism

ABSTRACT

The present study aimed to characterize cerebral morphology in young adult ferrets and its sexual dimorphism using high-field MRI and MRI-based morphometry. *Ex vivo* short TR/TE (typical T_1-weighted parameter setting for conventional MRI) and T_2W (long TR/TE) MRI with high spatial resolution at 7-tesla could visualize major subcortical and archicortical structures, i.e., the caudate nucleus, lentiform nucleus, amygdala and hippocampus. In particular, laminar organization of the olfactory bulb was identifiable by short TR/TE-MRI. The primary and secondary sulci observable in the adult ferret were distinguishable on either short TR/TE- or T_2W-MRI, and the cortical surface morphology was reproduced well by 3D-rendered images obtained by short TR/TE-MRI. The cerebrum had a significantly lower volume in females than in males, which was attributed to region-specific volume reduction in the cerebral cortex and subcortical white matter in females. A sexual difference was also detected, manifested by an overall reduction in normalized signal ratios of short TR/TE-MRI in all cerebral structures examined in females than in males. On the other hand, an alternating array of higher and lower short TR/TE-MRI intensity transverse zones throughout the cortex, which was reminiscent of the functional cortical areas, was revealed by maximum intensity projection (MIP) in 3D. The normalized signal ratio of short TR/TE-MRI, but not T_2W-MRI in the cortex, was negatively correlated with the density of myelin-basic protein immunoreactive fibers (males, $r = -0.440$; females, $r = -0.481$). The present results suggest that sexual differences in the adult ferret cerebrum are characterized by reduced volumes of the cerebral cortex and subcortical white matter in females, and by overall reductions in physiochemical characteristics, as obtained by short TR/TE-MRI, in females. It should be noted that short TR/TE-MRI-based MIP delineated functional cortical areas related to myeloarchitecture in 3D. Such an approach makes possible conventional investigation of the functional organization of the cerebral cortex and its abnormalities using high-field MRI.

Abbreviations: A1, primary auditory cortex; aad, anterior ancinate dimple; AAF, anterior auditory field; ac, anterior commissure; aci, intrabulbar anterior commissure; ADF, anterior dorsal field; as, ancinate sulcus; AEG, anterior ectosylvian gyrus; ASG, anterior sigmoid gyrus; Amg, amygdala; AVF, anterior ventral field; cc, corpus callosum; Cd, caudate nucleus; cg, cingulum; CNG, coronal gyrus; cns, coronal sulcus; crs, cruciate sulcus; csss, caudal suprasylvian sulcus; ec, external capsule; EPl, external plexiform layer; Gl, glomerular layer; Hip, hippocampus; ic, internal capsule; IPl, internal plexiform layers; LG, lateral gyrus; Ln, lentiform nucleus; ls, lateral sulcus; M1, primary motor cortex; MBP, myelin basic protein; Mi, mitral layer; MIP, maximum intensity projection; Ob, olfactory bulb; Obc, olfactory bulb core; OBG, orbital gyrus; OD, optical density; opr, optic radiation; ots, occipitotemporal sulcus; oSVZ, outer subventricular zone; PEG, posterior ectosylvian gyrus; PFA, paraformaldehyde; PPr, rostral posterior parietal cortex; prs, presylvian sulcus; PPF, posterior pseudosylvian field; prs, presylvian sulcus; PSF, posterior suprasylvian field; PSG, posterior sigmoid gyrus; pss, pseudosylvian sulcus; rf, rhinal fissure; rs, rhinal sulcus; rsss, rostral suprasylvian sulcus; spt, septum; S1, primary somatosensory cortex; SII, secondary somatosensory cortex; SIII, third somatosensory cortex; SSG, suprasylvian gyrus; subWM, subcortical matter; ss, splenial sulcus; Th, thalamus; VCA, visual cortical area.

* Corresponding author at: Department of Physical Therapy, Faculty of Medical and Health Sciences, Tsukuba International University, 6-8-33 Manabe, Tsuchiura, Ibaraki 300-0051, Japan. Fax: +81 29 826 6776.
E-mail address: k-sawada@tius-hs.jp (K. Sawada).

1053-8119/$ – see front matter © 2013 Elsevier Inc. All rights reserved.
http://dx.doi.org/10.1016/j.neuroimage.2013.06.024

Introduction

The remarkable development and spread of imaging techniques such as MRI and CT in recent years have provided full 3D brain coverage, while leaving the gross anatomy conserved. Quantitative analysis methods using these imaging techniques allow the investigation of focal differences in brain structures between a control and experimental group, or time-dependent changes in brain structures within groups (Wright et al., 1995). A number of studies have been attempted to explain structural sexual dimorphism of brain regions, quantitatively. Sex differences are noted in volumes of particular regions of the cerebral cortex, hippocampus, caudate nucleus, globus pallidus and/or olfactory bulb in humans (Carne et al., 2006; Giedd et al., 1997; Suzuki et al., 2005) and mice (Schlaepfer et al., 1995; Spring et al., 2007). Several studies revealed that sex-related volume changes in specific regions of the brain are involved in neurodevelopmental and psychological disorders such as schizophrenia (Exner et al., 2008), amnestic mild cognitive impairment, Alzheimer's disease

(Skup et al., 2011), and panic disorder (Asami et al., 2009) in humans. In addition, a higher prevalence of autism is found in males than in females, and appears to show abnormalities in the cerebral cortical surface morphology (Harden et al., 2004; Levitt et al., 2003). Therefore, quantitative data regarding sexual dimorphism of various regions provide fundamental information for investigating the pathogenesis of sex-related neurodevelopmental and psychological disorders.

Ferrets (*Mustela putorius*) are the smallest laboratory animals that have a highly convoluted surface of the cerebrum, forming striking patterns of sulci and gyri (Lawes and Andrews, 1998). This animal has advantages as an experimental model for studying the plasticity and development of the central nervous system. Neurodevelopmental events occurring *in utero* in primates, such as the early stage of neurogenesis (Clancy et al., 2001), sulcal infolding (Sawada and Watanabe, 2012; Smart and McSherry, 1986), and the transient appearance of the outer subventricular zone (oSVZ) with basal radial glia (Fietz et al., 2010; Martínez-Cerdeño et al., 2012), are experienced in ferrets following birth. This means that experimental magnifications such as drug administration and stress loading can be applied directly to the pups. Furthermore, ferrets are used as an animal model for a debilitating respiratory disease, human influenza, because of their high sensitivity to infection by human influenza viruses and diseases closely resembling human influenza (Maher and DeStefano, 2004). This means that ferrets have the potential for application to studies of influenza-associated encephalopathy. The present study aimed to characterize the cerebral morphology in young adult ferrets and its sexual dimorphism using MRI-based morphometry. To achieve a sufficient resolution for determining individual structures, fixed forebrain was examined using a high spatial resolution 7-tesla MRI system.

Materials and methods

Samples

The present study used cerebra from male and female ferrets at postnatal day (PD) 90 (male, n = 5; female, n = 5) that had been previously used in our gross anatomical examination of cerebral surface morphology (Sawada and Watanabe, 2012). Briefly, the animals were deeply anesthetized with an intraperitoneal injection of chloral hydrate (400 μg/g body weight), and were perfused with 0.9% NaCl followed by 4% paraformaldehyde (PFA) in a 10 mM phosphate buffer, pH 7.4. Brains were removed from skulls, and immersed in the same fixative.

MRI measurements

Three-dimensional T_1-weighted (short TR/TE) and two-dimensional T_2W (long TR/TE) MRI were performed with a 7.0-T MRI system (Magnet; Kobelco and Jastec, Kobe, Japan) (Console; Bruker BioSpin, Ettlingen, Germany). A birdcage RF coil for transmission and reception (70-mm inner diameter, Rapid Biomedica; or 60-mm inner diameter, Bruker BioSpin) was used with a field of view adequate for the sample dimensions. Slice orientation (transaxial) was precisely adjusted for the cerebral base using pilot-MR images obtained by gradient-echo sequence. A three-dimensional T_1-weighted image covering the entire brain was acquired using the rapid acquisition with relaxation enhancement (RARE) sequence, with the following parameters: repetition time (TR) = 300 ms, echo time (TE) = 9.6 ms (effective TE = 19.2 ms), RARE factor = 4, field of view (FOV) = 32 × 32 × 40 mm^3, acquisition matrix = 256 × 256 × 256, voxel size = 125 × 125 × 156 μm^3, number of acquisitions (NEX) = 2, and total scan time = 2 h 43 min 50 s. A multi-slice T_2-weighted image covering the entire brain was acquired using the RARE sequence with the following parameters: repetition time TR = 4200 ms, TE = 12 ms (effective TE = 36 ms), rare factor = 8, FOV = 38.4 × 38.4 mm^2, slice thickness = 1.0 mm, slice gap = 1.5 mm, number of slices = 10, acquisition matrix = 256 × 192 (reconstructed to 256 × 256 using zero-filling method), voxel size = 150 × 150 × 1000 μm^3, NEX = 40, and total scan time = 1 h 7 min 12 s.

We used the term "short TR/TE MRI" in the context of "MRI measured using typical T_1W parameter setting" in the present study, because the T_1W parameter setting did not show T_1-weighted contrast at the PFA-fixed brain sample under high-field MRI. Although shorter T_1 tissue, such as white matter, must be enhanced on T_1W-MRI, the signal was reduced due to the short T_2 of PFA solution (Supplement 1).

3D volume-rendered images

All 3D data were used for volumetric analysis. The cerebral cortex, olfactory bulb, caudate nucleus, lentiform nucleus (putamen plus globus pallidus), amygdala and hippocampus were semi-automatically segmented on MRI images using the "Morpho" tool of SliceOmatic software ver 4.3 (TomoVision, Montreal, Canada) based on image contrast as well as the user's knowledge of the anatomy. Segmented images were then analyzed using the 3D-rendering module of the same software. The cerebral image was rendered in 3D using the surface projection algorithm which best visualized the surface and sulci of the cerebrum. The 3D-rendered images were then rotated and manipulated in a manner that best visualized brain morphology by a linear registration method using SliceOmatic software. A clear indentation at the cerebral surface was considered the indication of a sulcus. A gyrus was defined as any tissue delimited by two or more fissures, sulci, or dimples. The terminology and identification of cerebral sulci and gyri were based on the textbook of Lawes and Andrews (1998).

Volumetric analysis

Areas of the segmented regions of each cerebral region were measured using SliceOmatic software. The volumes were calculated by multiplying the combined areas by the slice thickness (156.25 μm) with the total areas of those regions being regarded as the volume of the whole cerebrum. Data on the volume of each cerebral structure of the left and right hemispheres were analyzed separately.

Data analysis of short TR/TE and T_2W-MRI

Signal levels of short TR/TE and T_2W-MRI intensity were quantified by specifying the region of interest (ROI) in the known cortical areas, and in the major subcortical and archicortical structures. The following cortical regions were selected on the maximum intensity projection (MIP) color map by registration using the "Point" tool of SliceOmatic software for specifying the ROI, and signal intensities in each ROI: the primary motor cortex (M1; the rostral halves of posterior sigmoid gyrus (PSG) and coronal gyrus (CNG)), secondary somatosensory cortex (SII; the rostral half of the anterior ectosylvian gyrus (AEG)), primary auditory cortex (A1; the upper half of posterior ectosylvian gyrus (PEG)) as the cortical areas exhibiting a relatively low short TR/TE intensity, primary somatosensory cortex (S1; the caudal halves of PSG and CNG), rostral posterior parietal cortex (PPr; the rostral half of lateral gyrus (LG)), and area 17 (the caudal half of the visual cortical area (VCA)) as the cortical areas exhibiting a relatively high short TR/TE-MRI intensity. Intensities of short TR/TE- and T_2W-MRI were measured as background signals in the medium (4% PFA solution) that filled the brains. We defined the ROIs for the background signal at the points nearest (within 2–10 mm apart on the same coronal images) of ROIs for each brain region, in order to minimize the effect of RF inhomogeneity. Typical localizations of ROIs in each brain region and the respective background signals are shown in Supplement 2. The normalized signal ratios of short TR/TE and T_2W-MRI intensity were calculated by a formula [(signal intensity in the brain region) / (signal intensity of the nearest medium)]. Here, we carefully assessed the RF coil inhomogeneity (B_1 profile;

see Supplement 3). In our measurement conditions, inhomogeneity in the RF coil's B_1 field was very low in both T_1W (short TR/TE) MRI intensity (S.D. ratio = 0.0226) and T_2W-MRI intensity (S.D. ratio = 0.0479), suggesting that there was no serious signal inhomogeneity at the ROIs both in the brain and background medium. S.D. ratio indicates [(standard deviation of all ROIs)/(mean of all ROIs)].

Furthermore, the normalized signal ratios of short TR/TE and T_2W-MRI intensity were represented on coronal and axial images using a color-scale ("gray level intensity color map" module, SliceOmatic software).

A MIP color map was made from the segmented images of the cerebral cortex on short TR/TE MRI using the MIP module of the

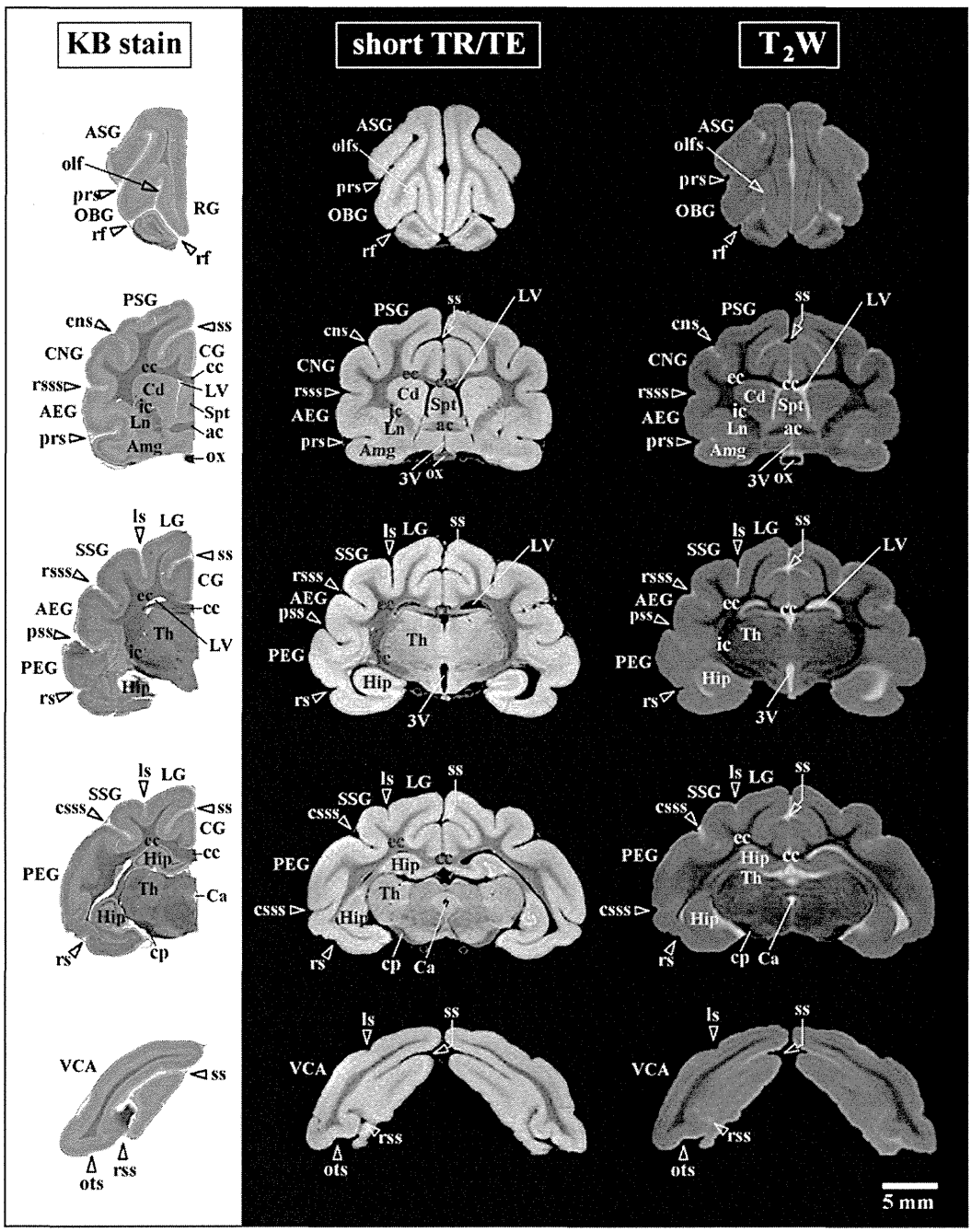

Fig. 1. Representative coronal short TR/TE-MRI (typical T_1-weighted parameter setting for conventional MRI) and T_2W-MRI (long TR/TE) images of adult male ferret cerebrum with identical planes of Klüver–Barrera stained sections. (A) Klüver–Barrera stained sections, (B) short TR/TE-MRI images, and (C) T_2W-MRI images. Both short TR/TE- and T_2W-MRI visualized major subcortical and archicortical structures, and all primary sulci and dimples. The T_1W parameter setting (short TR/TE) did not show T_1-weighted contrast at the PFA-fixed brain sample under high-field MRI in the present study. Although shorter T_1 tissue, such as white matter, must be enhanced on T_1W-MRI, the signal was reduced due to the short T_2 of PFA solution (Supplement 1). 3V, third ventricle; ac, anterior commissure; AEG, anterior ectosylvian gyrus; Amg, amygdala; as, ancinate sulcus; ASG, anterior sigmoid gyrus; Ca, cerebral aqueduct; cc, corpus callosum; Cd, caudate nucleus; CG, cingulate gyrus; CNG, coronal gyrus; cns, coronal sulcus; cp, cerebral peduncle; csss, caudal suprasylvian sulcus; ec, external capsule; Hip, hippocampus; ic, internal capsule; LG, lateral gyrus; Ln, lentiform nucleus; LV, lateral ventricle; OBG, orbital gyrus; olf, olfactory sulcus; ots, occipitotemporal sulcus; ox, optic chiasma; PEG, posterior ectosylvian gyrus; PFA, paraformaldehyde; prs, presylvian sulcus; PSG, posterior sigmoid gyrus; rf, rhinal fissure; RG, rectal gyrus; rsss, rostral suprasylvian sulcus; rs, rhinal sulcus; spt, septum; ss, splenial sulcus; SSG, suprasylvian gyrus; Th, thalamus; VCA, visual cortical area.

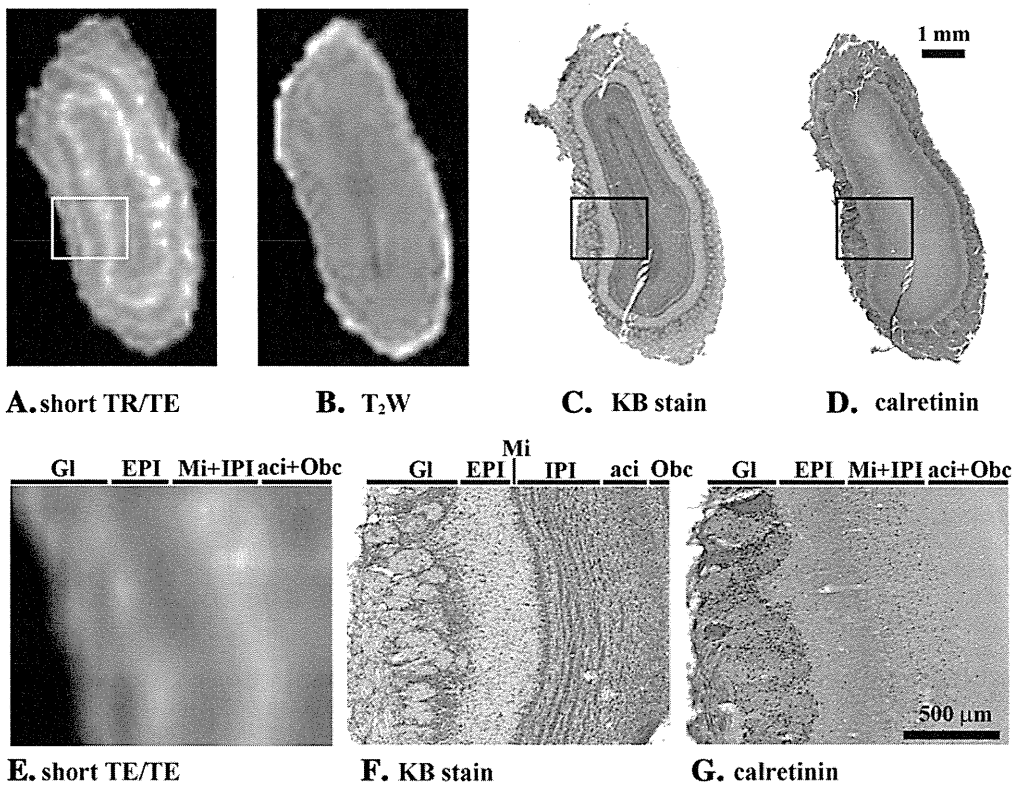

Fig. 2. Representative short TR/TE-MRI (typical T_1-weighted parameter setting for conventional MRI) and T_2W-MRI (long TR/TE) images of olfactory bulb of adult male ferrets with identical planes of Klüver–Barrera stained and calretinin-immunostained sections. (A) Short TR/TE-MRI image, (B) T_2W-MRI image, (C) Klüver–Barrera stained section, and (D) calretinin-immunostained section. (E) Boxed areas of short TR/TE-MRI image of (A) at high magnification. (F) Boxed areas of Klüver–Barrera stained and section of (C) at high magnification. (G) Boxed areas of calretinin-immunostained section of (D) at high magnification. The T_1W parameter setting (short TR/TE) did not show T_1-weighted contrast at the PFA-fixed brain sample under high-field MRI in the present study. Although shorter T_1 tissue, such as white matter, must be enhanced on T_1W-MRI, the signal was reduced due to the short T_2 of PFA solution (Supplement 1). Some layers of olfactory bulb were distinguishable by short TR/TE-MRI. aci, intrabolbar acinar commissure; EPI, external plexiform layer; Gl, glomerular layer; IPI, internal plexiform layer; Mi, mitral layer; Obc, olfactory bulb core, PFA, paraformaldehyde.

SliceOmatic software. MIP is a volume visualization method for 3D data that projects in the visualization plane the voxels with the maximum intensity that fall in the way of parallel rays traced from the viewpoint to the plane of projection.

Histology and immunohistochemistry

Following MRI measurements, right and left cerebral hemispheres were separated at the longitudinal cerebral fissure, and were cryoprotected by

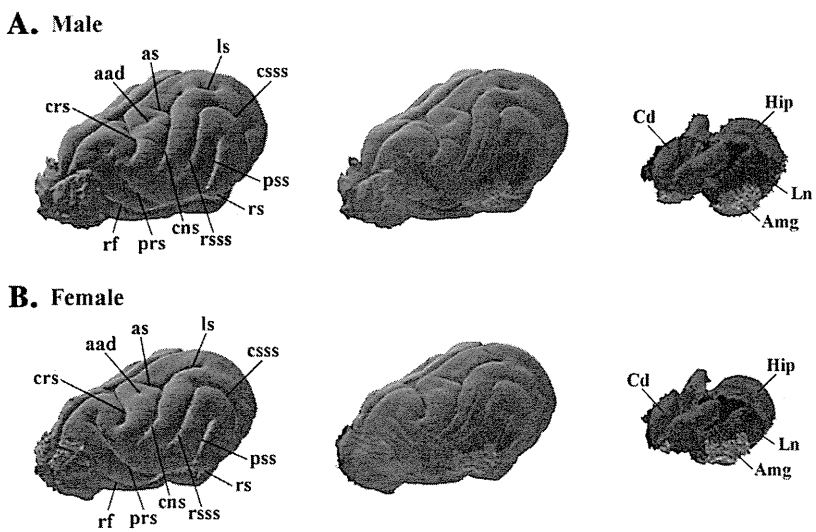

Fig. 3. Volume-rendered images in cerebra of male and female ferrets. (A) Three-dimensional volume-rendered images of male cerebrum. (B) Three-dimensional volume-rendered images of female cerebrum. Left images of (A) and (B) are reconstructed images of cerebral cortex and olfactory bulb (Ob); middle images of (A) and (B) are reconstructed images of all cerebral structures rendered. Right images of (A) and (B) are reconstructed images of caudate nucleus (Cd; red), lentiform nucleus (Ln; blue), amygdala (Amg; green) and hippocampus (Hip; purple). aad, anterior ancinate dimple; as, ancinate sulcus; cns, coronal sulcus; crs, cruciate sulcus; csss, caudal suprasylvian sulcus; prs, presylvian sulcus; pss, pseudosylvian sulcus; rf, rhinal fissure; rs, rhinal sulcus; rsss, rostral suprasylvian sulcus; subWM, subcortical matter.

immersion in 30% sucrose in 10 mM phosphate-buffered saline (PBS) overnight. The cerebral hemispheres were frozen in optimal cutting temperature embedding compound, and sectioned serially in the coronal plane at 40 μm by a Retratome (REM-700; Yamato Koki Industrial, Asaka, Japan) with a refrigeration unit (Electro Freeze MC-802A, Yamato Koki Industrial Co., Ltd.). Some sections were stained with Klüver–Barrera according to protocols of Sheehan and Hrapchak (1980) as an anatomical reference to MRI images.

All immunohistochemical procedures were performed on floating sections. The sections were immersed in 3% H_2O_2 in PBS containing 0.1% Triton X-100 for the inactivation of endogenous peroxidase. After washing with PBS, sections were reacted with a rabbit anti-calretinin polyclonal antibody (1:10,000; Swant, Switzerland), or a rat anti-myelin basic protein (MBP) monoclonal antibody (Millipore, Billerica, CA, USA), containing 10% normal goat serum at 4 °C overnight. Those two antibodies produced highly specific immunostaining in the ferret tissues in previous studies (Poluch et al., 2008; Tao et al., 2012). After incubation, the sections were rinsed with PBS and reacted with biotinylated anti-rabbit IgG or biotinylated anti-rat IgG. The immunoreactive products were visualized by a Vectastain ABC elite kit (Vector Labs., Inc., Burlingame, CA) using 0.01% 3,3′-diaminobenzidine tetrachloride (Sigma) in 0.03% H_2O_2 as a chromogen.

To enable a comparison of MBP immunoreactive fiber density, all sections were processed in identical staining conditions. Evaluation of MBP immunoreactive fibers in the cerebral cortex was performed by using a modified protocol designed for our previous study (Koyanagi et al., 2006). Captured images of the MBP immunostained sections of the identical regions of the cortex, which were used to calculate the normalized ratios of short TR/TE- and T_2W-MRI intensity in the primary motor cortex (M1; the rostral halves of PSG and CNG), primary somatosensory cortex (S1; the caudal halves of PSG and CNG), secondary somatosensory cortex (SII; the rostral half of the AEG), primary auditory cortex (A1; the upper half of PEG), rostral posterior parietal cortex (PPr; the rostral half of LG), and area 17 (the caudal half of the VCA), were converted to black and white images. The optical density (OD) within a rectangular frame at a width of 200 μm and a length covering the entire depth of the cortex was measured in each cortical area as the MBP immunoreactive fiber density using ImageJ software (National Institutes of Health, Bethesda, USA). The mean of five points more than 30 μm apart was used for each animal when measuring the OD.

Table 1
Absolute volumes, % of total cerebral volume, and % larger in male volumes of cerebral structures in ferrets.

	n=	Absolute volume (mm^3)	% of total cerebral volume	% larger in male volumes
Cerebrum				
Male	10	2,139 ± 113.1#	–	10.8
Female	10	1,930 ± 117.4	–	–
Cortex				
Male	10	1,317 ± 92.0***	61.5 ± 1.45***	8.4
Female	10	1,214 ± 80.5	62.9 ± 0.69	–
Olfactory bulb				
Male	10	104 ± 9.0	4.9 ± 0.52	6.4
Female	10	98 ± 6.2	5.1 ± 0.36	–
Caudate nucleus				
Male	10	62 ± 3.4	2.9 ± 0.22	7.9
Female	10	58 ± 3.3	3.0 ± 0.16	–
Lentiform nucleus				
Male	10	62 ± 5.7	2.9 ± 0.30	17.0
Female	10	53 ± 4.3	2.7 ± 0.14	–
Amygdala				
Male	10	43 ± 2.7	2.0 ± 0.15	−0.9
Female	10	43 ± 3.6	2.2 ± 0.23	–
Hippocampus				
Male	10	93 ± 5.3	4.3 ± 0.32	11.7
Female	10	83 ± 7.7	4.3 ± 0.42	–
Subcortical white matter				
Male	10	312 ± 32.9**	14.6 ± 1.22*	15.4
Female	10	271 ± 23.8	14.0 ± 0.85	–

All measurements of the left and right hemispheres were quantified separately in males (n = 5) and females (n = 5), and data on each side were considered to be "n = 1."
Results of volumes of each cerebral structure and % of cerebral volume are presented as mean ± S.D. Results of % larger volumes in males than in females are presented.
# $P < 0.001$ vs. females (Student's *t*-test).
* $P < 0.05$ vs. females (*Fisher's* LSD test).
** $P < 0.01$ vs. females (*Fisher's* LSD test).
*** $P < 0.001$ vs. females (*Fisher's* LSD test).

Statistical analysis

All measurements of the left and right hemispheres were quantified separately. This was followed by a paired sampled *t*-test that demonstrated no significant left/right differences, and data on each side were considered to be "n = 1." Sex-related changes in each parameter were statistically evaluated by two-way ANOVA using both sexes and brain regions (gray and white matter structures or cortical areas) as factors. Then, as post-hoc testing, *Fisher's* LSD test was used to compare males and females.

Ethics

The experimental procedures in the present study were conducted in accordance with the guidelines of the National Institutes of Health (NIH) for the Care and Use of Laboratory Animals. The Institutional

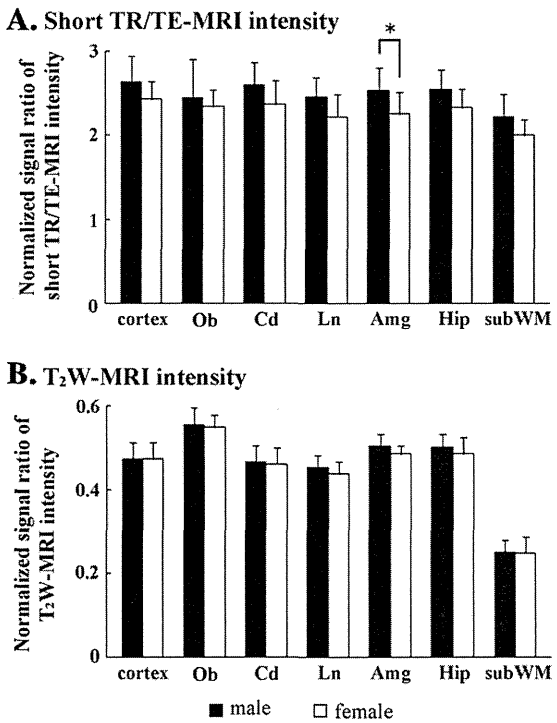

Fig. 4. Bar graphs for normalized signal ratios of short TR/TE (typical T_1-weighted parameter setting for conventional MRI) and T_2W (long TR/TE) MRI intensity in cerebral cortex, and subcortical and archicortical structures of male and female ferrets. Measurements of left and right hemispheres were quantified separately in males (n = 5) and females (n = 5), and data on each side of the hemispheres were considered to be "n = 1." (A) Normalized signal ratios of short TR/TE-MRI intensity. For short TR/TE-MRI, two-way ANOVA revealed significant effects on sexes ($F_{1,126} = 18.401$, $P < 0.001$) and cerebral structures ($F_{6,126} = 4.338$, $P < 0.001$), but not on their interaction. (B) Normalized signal ratios of T_2W-MRI intensity. For T_2W-MRI, two-way ANOVA revealed significant effects on cerebral structures ($F_{6,126} = 124.329$, $P < 0.001$), but not on sexes and their interaction. *: $P < 0.05$ (*Fisher's* LSD test). Amg, amygdala; Cd, caudate nucleus; Hip, hippocampus; Ln, lentiform nucleus; Ob, olfactory bulb; subWM, subcortical white matter.

Animal Care and Use Committee of Tsukuba International University approved the procedures, and all efforts were made to minimize the number of animals used and their suffering.

Results

Images of short TR/TE and T_2W-MRI

Representative images from coronal short TR/TE- and T_2W-MRI of adult male ferrets' cerebra were shown in Fig. 1. The T_1W parameter setting (short TR/TE) did not show T_1-weighted contrast at the PFA-fixed brain sample under high-field MRI in the present study. Although shorter T_1 tissue, such as white matter, must be enhanced on T_1W-MRI, the signal was reduced due to the short T_2 of PFA solution (Fig. 1, Supplement 1). Klüver–Barrera staining was conducted for anatomical reference. Both short TR/TE- and T_2W-MRI visualized major subcortical and archicortical structures, i.e., the caudate nucleus (Cd), the lentiform nucleus (Ln), the amygdala (Amg) and the hippocampus (Hip). Subcortical matter (SubWM), including a corpus callosum (cc) and external capsule (ec), was also delineated. The cerebral cortex was clearly distinguishable by having a relatively high signal intensity of short TR/TE- and T_2W-MRI compared to the adjacent white matter. All primary sulcus and dimples observed on gross observations previously (Sawada and Watanabe, 2012) were identifiable on either short TR/TE- or T_2W-MRI.

In the olfactory bulb (Ob), four layers with the higher and lower short TR/TE-MRI signals aligned alternately from the outer surface (Fig. 2). An observation of such an array of layers was unclear by T_2W-MRI (Fig. 2). In order to identify short TR/TE-MRI-defined layers of the olfactory bulb, MRI images were compared with the identical plane of Klüver–Barrera-stained sections. The outermost layers with high signal intensity and the second layer with low signal intensity corresponded to the glomerular layer (Gl) and the external plexiform layer (EPl), respectively. The third layer with high signal intensity was seen through the mitral (Mi) and internal plexiform layers (IPl). A boundary to those two layers was not delineated by short TR/TE-MRI. Likewise, the fourth layer with low signal intensity was seen through the white matter bundles of intrabulbar anterior commissure (aci) and the olfactory bulb core (Obc), with no demarcation of their boundary by short TR/TE-MRI. Furthermore, we carried out immunostaining for calretinin, which is a specific marker for interneurons of the Gl and IPl. Consistent with findings by Klüver–Barrera staining, the superficial and third layers representing higher short TR/TE-MRI signals corresponded to the Gl and IPl, which contained a high density of calretinin-immunoreactive small neurons (Fig. 2).

3D reconstruction and volumetric analysis

Three-dimensional volume-rendered images of the cerebrum of male and female ferrets were calculated using short TR/TE-MRI. The rendered images reproduced the cerebral cortical morphology well, with the primary and secondary sulci observable in the adult ferrets (Fig. 3). The cerebral volume was significantly lower in females than in males ($P < 0.001$) (Table 1). The 3D morphology and topology of major subcortical and archicortical structures, i.e., the olfactory bulb, caudate nucleus, lentiform nucleus, amygdala and hippocampus, were also obtained by the rendered images (Fig. 3). We calculated the volumes of those structures in male and female ferrets. Two-way ANOVA revealed significant effects on sexes ($F_{1,126} = 17.707$, $P < 0.001$) and cerebral structures ($F_{6,26} = 3298.686$, $P < 0.001$), and the interactions of those two factors ($F_{6,26} = 5.624$, $P < 0.001$). Region-specific sexual difference was detected by significantly lower volumes of cerebral cortex ($P < 0.001$) and subcortical white matter ($P < 0.01$) in females than males by post-hoc testing.

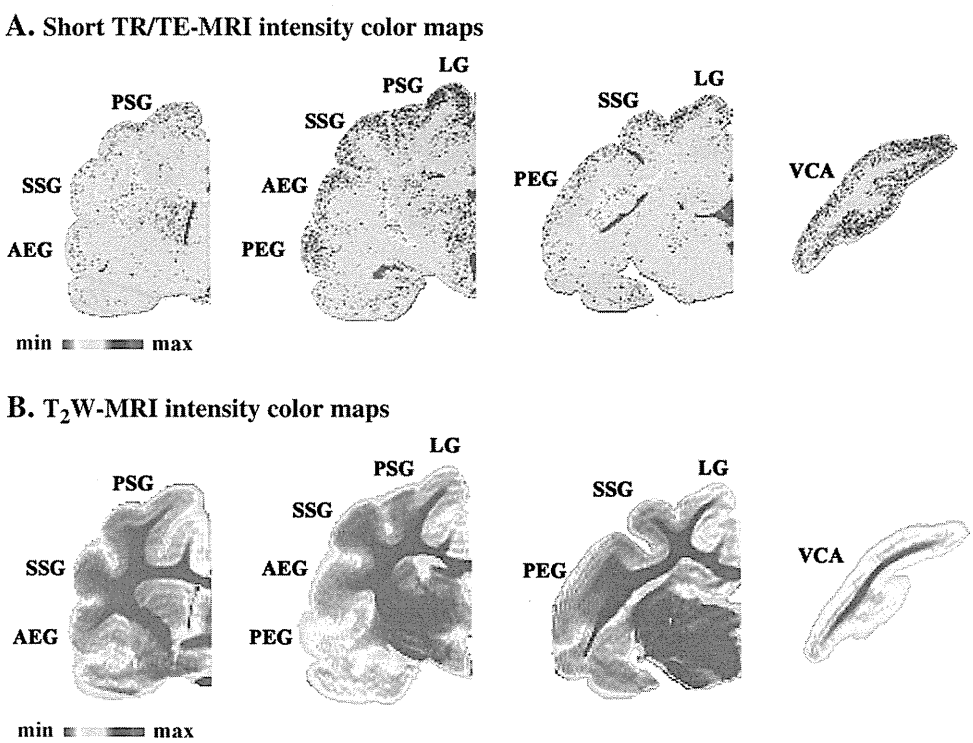

Fig. 5. Representative coronal images of short TR/TE (typical T_1-weighted parameter setting for conventional MRI) and T_2W (long TR/TE) MRI intensity color maps. (A) Short TR/TE-MRI intensity color maps of male ferret cerebrum. (B) T_2W-MRI intensity color maps of male ferret cerebrum. Signal intensities represented on short TR/TE- and T_2W-MRI images of each pixel were color-coded. The T_1W parameter setting (short TR/TE) did not show T_1-weighted contrast at the PFA-fixed brain sample under high-field MRI in the present study. Although shorter T_1 tissue, such as white matter, must be enhanced on T_1W-MRI, the signal was reduced due to the short T_2 of PFA medium (Supplement 1). AEG, anterior ectosylvian gyrus; LG, lateral gyrus; PEG, posterior ectosylvian gyrus; PSG, posterior sigmoid gyrus; SSG, suprasylvian gyrus; VCA, visual cortical area; PFA, paraformaldehyde.

In addition to the absolute volumes of cerebral structures, we conducted two approaches of volume data analyses considering the possibility of slight brain shrinkage by long-term fixation in the PFA solution. First, absolute volumes of each cerebral structure were normalized to the whole cerebral volume (results are shown in Table 1). Then, two-way ANOVA revealed significant effects on cerebral structures ($F_{6,26} = 234524.881$, $P < 0.001$) and interactions between sexes and cerebral structures ($F_{6,26} = 4.429$, $P < 0.001$). Significantly lower volumes of cerebral cortex ($P < 0.001$) and subcortical white matter ($P < 0.05$) in females than in males were detected by post-hoc testing. As with the results of the absolute volumes, the % volumes of other cerebral structures to total cerebral volumes were not different between sexes, statistically. Second, we calculated larger % volumes in males than in females (Table 1). While the volume of amygdala in females was almost equal to that in males, 6–17% larger volumes in males rather than in females were marked in other cerebral structures (the cortex, olfactory bulb, caudate nucleus, lentiform nucleus, hippocampus and subcortical white matter).

Normalized signal ratios of short TR/TE- and T_2W-MRI intensity in subcortical and archicortical structures

The signal intensities of short TR/TE- and T_2W-MRI were normalized in the cerebral cortex, the major subcortical (i.e., the caudate nucleus and lentiform nucleus) and archicortical structures (i.e., the olfactory bulb, amygdala and hippocampus), and in the subcortical white matter. The normalized signal ratio of the short TR/TE-MRI intensity in those structures was slightly higher in males than in females (Fig. 4). Two-way ANOVA revealed significant effects on sexes ($F_{1,126} = 18.401$, $P < 0.001$) and cerebral structures ($F_{6,126} = 4.338$, $P < 0.001$), but not on their interaction. Therefore, a reduction in the signal ratio of short TR/TE-MRI intensity was found throughout the female cerebrum while post-hoc testing indicated significantly higher signal ratios only in the amygdala. In contrast, the normalized signal ratio of the T_2W-MRI intensity in each structure did not differ between sexes (Fig. 4). Two-way ANOVA revealed significant effects on cerebral structures ($F_{6,126} = 124.329$, $P < 0.001$), but not on sexes and their interaction. The significant effects on the cerebral

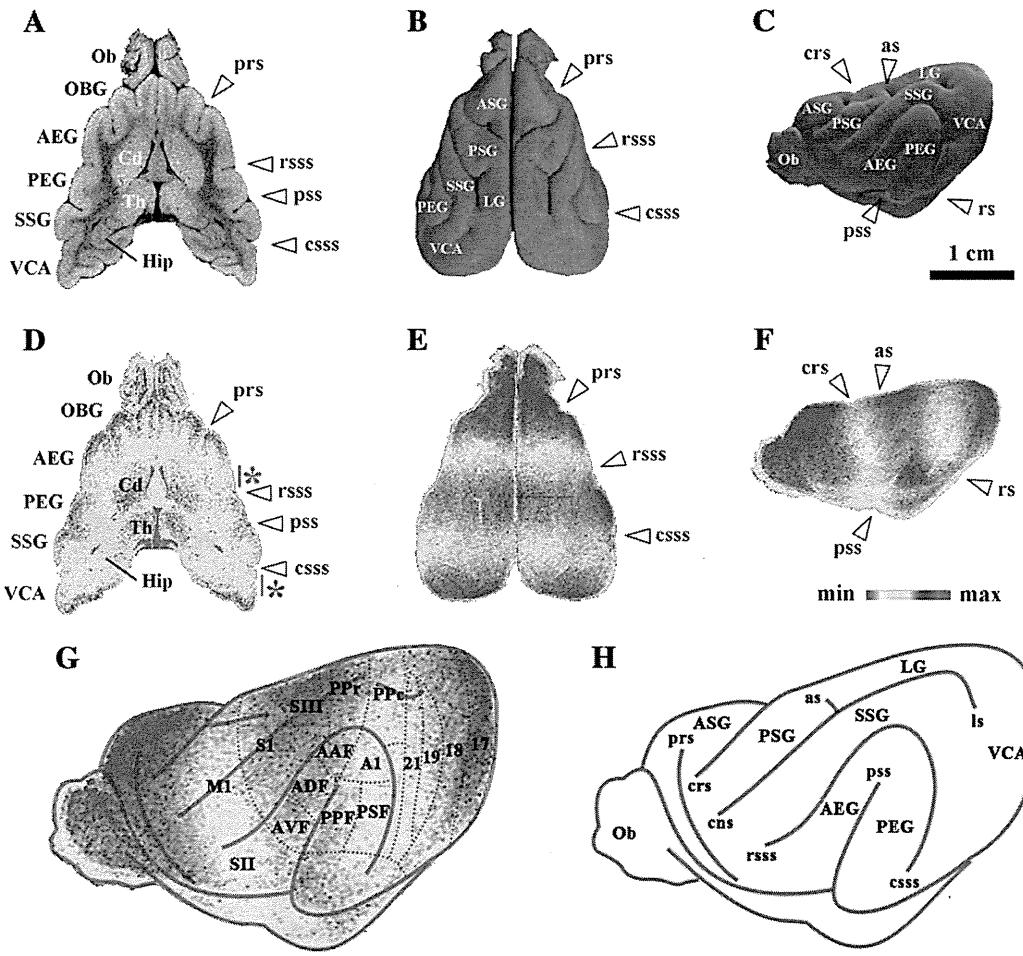

Fig. 6. Short TR/TE-MRI-based MIP color maps and axial image of short TR/TE-MRI color map representing an array of higher and lower short TR/TE-MRI transverse zones through the cerebral cortex. (A) Axial short TR/TE-MRI image of ferret cerebrum as a reference. (B) Dorsal view of three-dimensional volume-rendered images of cerebrum as a reference. (C) Lateral view (left side) of three-dimensional volume-rendered images of cerebrum as a reference. (D) Axial image of short TR/TE-MRI intensity color map of the cerebrum. Signal intensities represented on short TR/TE-MRI images of each pixel were color-coded. Red asterisks (*) in (D) indicate lower short TR/TE-MRI transverse zones of the cerebral cortex on axial short TR/TE-MRI images. (E) Dorsal view of short TR/TE-MRI-based MIP color map of the cerebrum. (F) Lateral view (left side) of short TR/TE-MRI-based MIP color map of the cerebrum. (G) Known functional cortical areas of cerebrum (modified from Manger et al., 2004; Keniston et al., 2009; Foxworthy and Meredith, 2011) overlayed on the lateral view of the MIP color map. An array of higher and lower short TR/TE-MRI transverse zones defined by MIP color map was reminiscent of the functional cortical areas. (H) Lateral view of sulcal and gyral map as a reference. A1, primary auditory cortex; AAF, anterior auditory field; ADF, anterior dorsal field; as, ancinate sulcus; AEG, anterior ectosylvian gyrus; ASG, anterior sigmoid gyrus; AVF, anterior ventral field; Cd, caudate nucleus; cns, coronal sulcus; crs, cruciate sulcus; csss, caudal suprasylvian sulcus; Hip, hippocampus; M1, primary motor cortex; Ob, olfactory bulb; OBG, orbital gyrus; PEG, posterior ectosylvian gyrus; PPc, caudal posterior parietal cortex; PPr, rostral posterior parietal cortex; prs, presylvian sulcus; PSG, posterior sigmoid gyrus; pss, pseudosylvian sulcus; rs, rhinal sulcus; rsss, rostral suprasylvian sulcus; S1, primary somatosensory cortex; SII, second somatosensory cortex; SIII, third somatosensory cortex; SSG, suprasylvian gyrus; Th, thalamus; VCA, visual cortical area.

structures revealed that signal ratios of short TR/TE- and T_2W-MRI intensity were different among each cerebral structure. Subcortical white matter, the sole white matter structure examined in the present study, was noted for having lower signal ratios of short TR/TE- and T_2W-MRI intensity than signal ratios of other cerebral structures of male and female ferrets.

Color maps of short TR/TE- and T_2W-MRI intensity and short TR/TE-MRI-based MIP

Short TR/TE- and T_2W-MRI represent the physiochemical properties of the tissues that differ among each structure of the cerebrum. Coronal images of short TR/TE- and T_2W-MRI color maps, and axial

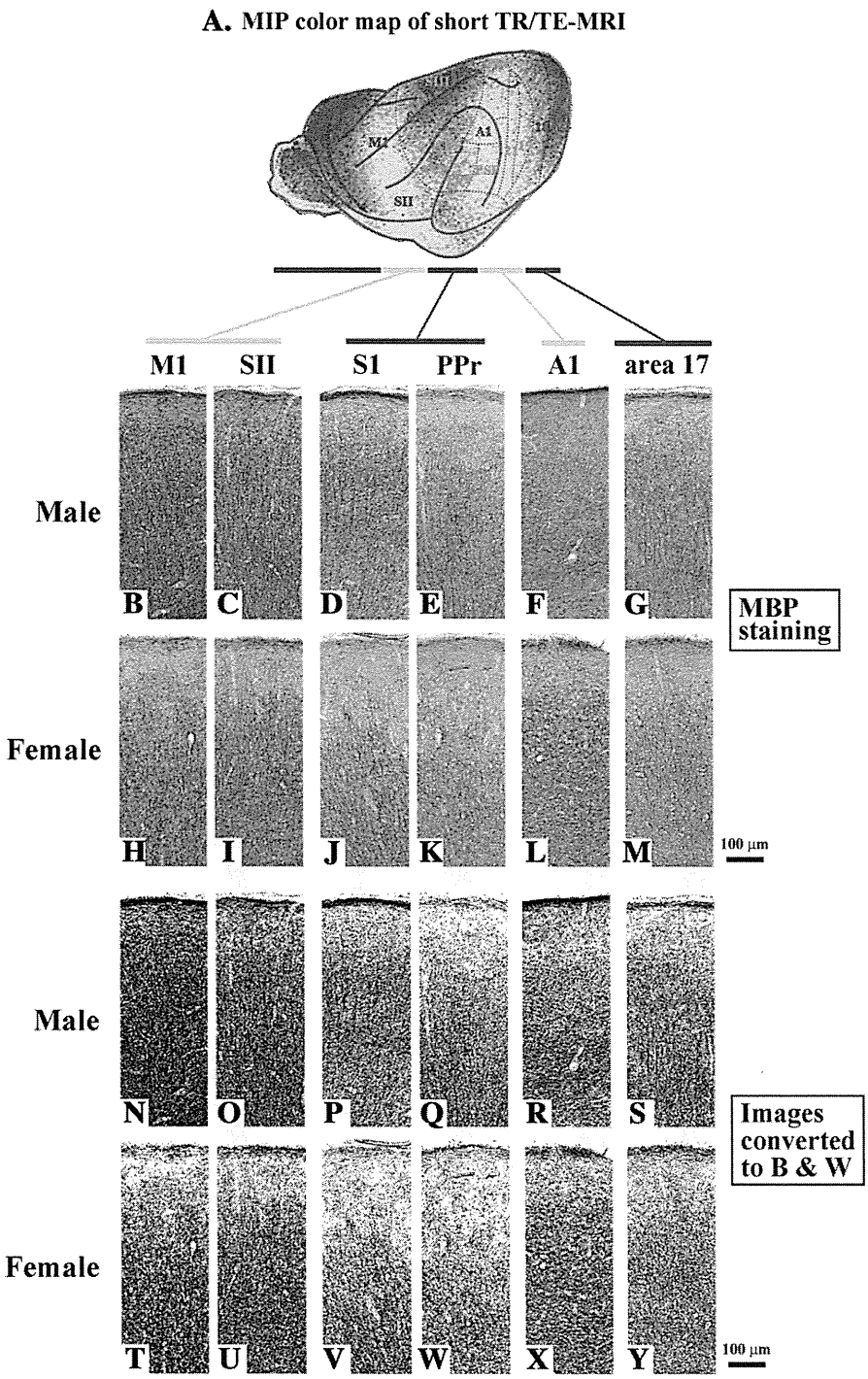

Fig. 7. Myelin basic protein (MBP) immunostaining in representative functional cortical areas of male and female ferrets. (A) Topology of each cortical area is shown by short TR/TE-MRI-based MIP color map of cerebral cortex. Photomicrographs from (B) to (M) are representative MBP-immunostained sections of rostral lower intensity zone (primary motor cortex (M1) and second somatosensory cortex (SII)), intermediate higher intensity zone (primary somatosensory cortex (S1) and rostral posterior parietal cortex (PPr)), caudal lower intensity zone (primary auditory cortex (A1)), and caudal higher intensity zone (area 17) of male (B–G) and female (H–M) ferrets. Photomicrographs in (N) to (Y) are images of MBP-immunostained sections in each cortical area converted into black and white for evaluating the density of MBP immunoreactive fibers of male (N–S) and female (T–Y) ferrets. AAF, anterior auditory field; ADF, anterior dorsal field; AVF, anterior ventral field; PPc, caudal posterior parietal cortex; SIII, third somatosensory cortex.

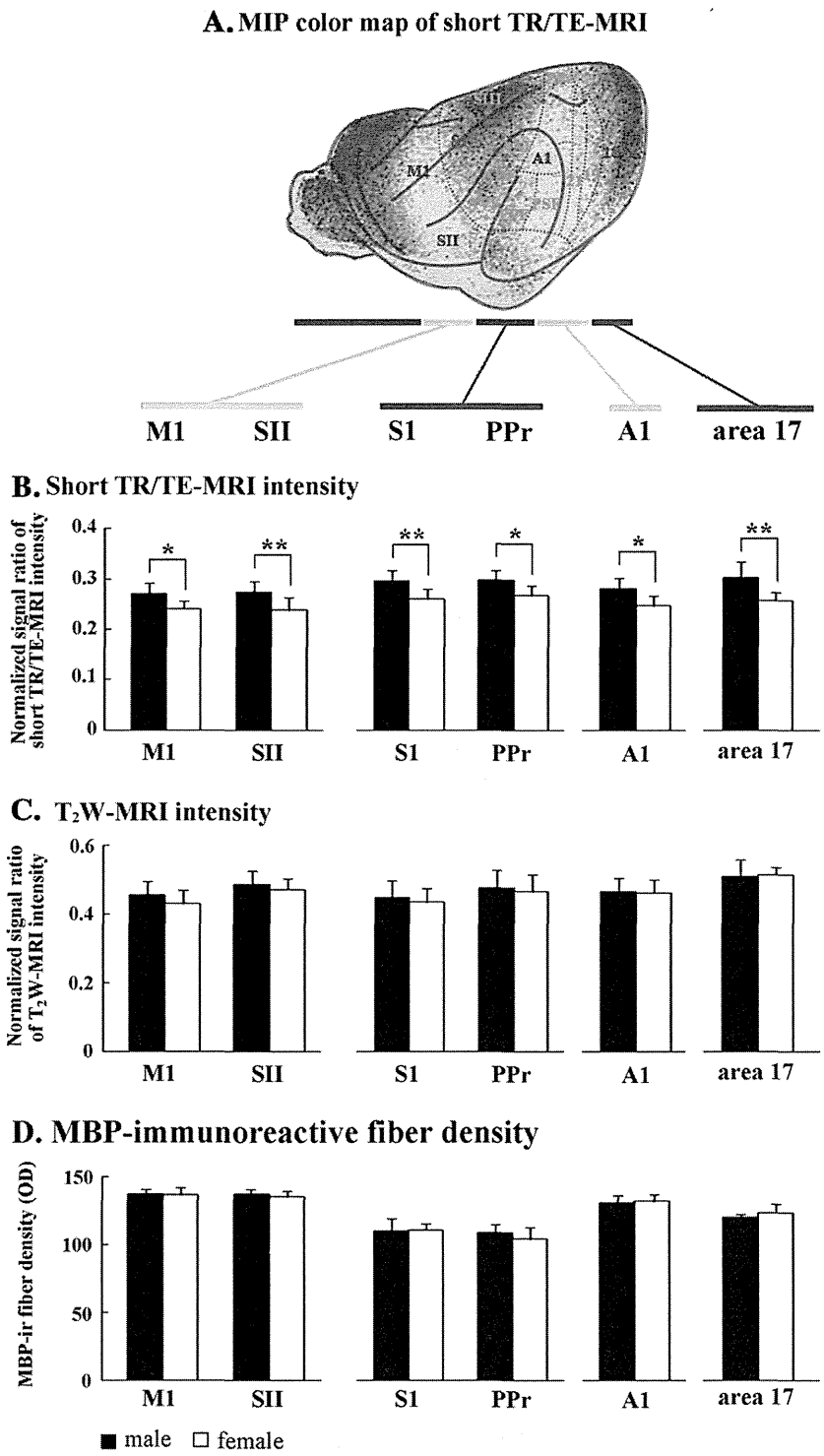

Fig. 8. Bar graphs for normalized signal ratios of short TR/TE (typical T_1-weighted parameter setting for conventional MRI) and T_2W (long TR/TE) MRI intensity, and for the density of myelin basic protein (MBP) immunoreactive (ir) fibers of representative cortical areas of male and female ferrets. Measurements of the left and right hemispheres were quantified separately, and data on each side of the hemisphere were considered to be "n = 1." (A) Topology of each cortical area is shown by short TR/TE-MRI-based MIP color map of the cerebral cortex: primary motor (M1) and second somatosensory (SII) cortices located in the rostral lower intensity zone; the primary somatosensory (S1) and rostral posterior parietal (PPr) cortices located in the intermediate higher intensity zone; primary auditory cortex (A1) located in the caudal lower intensity zone; and area 17 located in the caudal higher intensity zone. (B) Normalized signal ratios of short TR/TE-MRI intensity. For short TR/TE-MRI, two-way ANOVA revealed significant effects on sexes ($F_{1,108} = 272.010$, $P < 0.001$) and cortical areas ($F_{5,108} = 5.718$, $P < 0.001$), but not on their interaction. *: $P < 0.01$; $P < 0.001$ (*Fisher's* LSD test). (C) Normalized signal ratios of T_2W-MRI intensity. For T_2W-MRI, a significant effect was found on cortical areas ($F_{5,108} = 7.400$, $P < 0.001$), but not on sexes or interactions between cortical areas and sexes. (D) MBP-ir fiber density. With MBP immunostaining, two-way ANOVA revealed a significant effect on cortical areas ($F_{1,108} = 97.043$, $P < 0.001$), but not on sexes or interactions between cortical areas and sexes.

images of short TR/TE-MRI color maps of the male ferret cerebrum are shown in Figs. 5 and 6, respectively. Short TR/TE-MRI intensity but not T_2W-MRI intensity was organized into an alternating array of higher and lower intensity transverse zones throughout the cerebral cortex. Short TR/TE-MRI intensity in both the rostral half of the AEG and the rostral half of the VCA was relatively lower than that in other cortical regions on those axial images (* in axial image of short TR/TE-MRI color map in Fig. 6D).

Spatial distributions of the cortical regions representing higher or lower short TR/TE-MRI intensity were examined by MIP, which projected the voxels with maximum intensity in 3D. The short TR/TE-MRI-based MIP color maps revealed an alternating array of higher and lower intensity transverse zones throughout the cerebral cortex in males (Fig. 6). A similar transverse array was obtained in the female cortex. In order to determine whether such an array is the effect of inhomogeneity in the RF coil's B_1 field, we examined the MIP color map of the background signal of the medium (PFA solution) that filled the brains. No stripes of higher or lower intensity were obtained through the medium on the MIP map (see Supplement 4), suggesting that B_1 field inhomogeneity is not responsible for the observed patterns. The lower intensity transverse zones were present through the rostral one-third regions of the PSG, suprasylvian gyrus (SSG) and AEG, and through the caudal half of the PEG and the caudal half of the VCA. The known cortical areas of the ferret cerebrum (modified from Foxworthy and Meredith, 2011; Keniston et al., 2009; Manger et al., 2004) were overlayed on the present MIP color maps in Fig. 6G. The rostral lower intensity transverse zone corresponded to the M1 and SII, and the caudal lower intensity transverse zone corresponded to the A1 (Fig. 6G).

Myelin fiber density and normalized signal ratios of short TR/TE- and T_2W-MRI intensity in cortical areas

Since the signal intensity of T_1-weighted MRI through the shortening of T_1 (longitudinal relaxation time) and T_2 (transverse relaxation time) is known to be altered by myelination (Holland et al., 1986), MBP immunostaining was carried out to evaluate the degree of myelination in each cortical area. A number of MBP-immunoreactive fibers were present in the cerebral cortex, while their densities varied among the cortical areas (Fig. 7). In order to quantify the density of those fibers, captured images were converted to black and white images (Fig. 7), and the OD was measured. Two-way ANOVA revealed a significant effect on cortical areas ($F_{1,108} = 97.043$, $P < 0.001$), but not on sexes in the density of MBP immunoreactive fibers. The density of MBP-immunoreactive fibers was relatively high in the M1, SII and A1, but relatively low in the S1, PPr, and area 17 (Fig. 8).

Normalized signal ratios of the short TR/TE-MRI intensity on each cortical area were shown in Fig. 8. Two-way ANOVA revealed significant effects on sexes ($F_{1,108} = 272.010$, $P < 0.001$) and cortical areas ($F_{5,108} = 5.718$, $P < 0.001$). Post-hoc testing indicated significantly lower signal ratios in females than in males throughout cortical areas examined, i.e., the M1 ($P < 0.01$), S1 ($P < 0.001$), SII ($P < 0.001$), A1 ($P < 0.01$), PPr ($P < 0.01$), and area 17 ($P < 0.001$) (Fig. 8). Such sexual differences were not region-specific, because there was no interaction

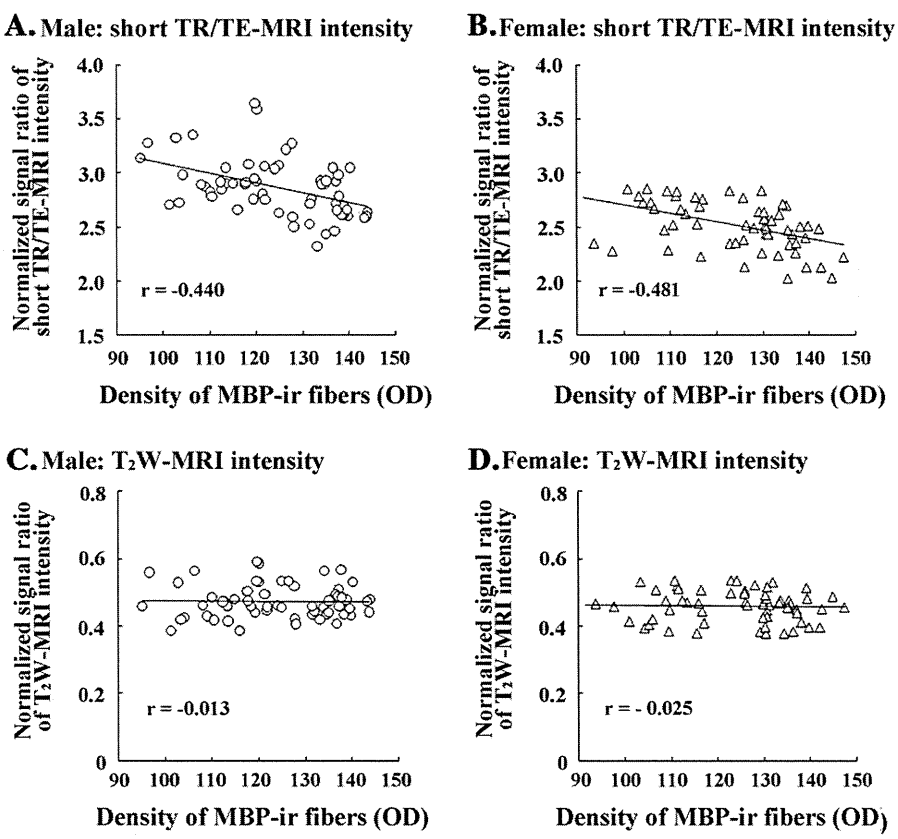

Fig. 9. Correlations of the density of myelin basic protein (MBP) immunoreactive (ir) fibers with normalized signal ratios of short TR/TE (typical T_1-weighted parameter setting for conventional MRI) and T_2W (long TR/TE) MRI in the cerebral cortex of ferrets. Measurements of left and right hemispheres were quantified separately in males (n = 5) and females (n = 5), and data on each side of the hemisphere were considered to be "n = 1." Since the ROIs were specified at 6 known cortical areas (i.e., the primary motor cortex (M1), primary somatosensory cortex (S1), secondary somatosensory cortex (SII), primary auditory cortex (A1), rostral posterior parietal cortex (PPr) and area 17), data obtained from total 60 points were plotted as circles or triangles in each graph (Y-axis: normalized signal ratio of short TR/TE- or T_2W-MRI intensity in each cortical area. X-axis: OD of MBP-ir fibers in identical cortical areas). Short TR/TE-MRI had a close negative correlation with the density of MBP immunoreactive fibers (males, r = −0.440; females, r = −0.481), but T_2W-MRI (males, r = 0.013; females, r = −0.025) did not.

between sexes and cortical areas by two-way ANOVA. It should be noted that signal ratios of short TR/TE-MRI intensity were different among cortical areas in both sexes. Relatively higher intensities, marked in the S1, PPr, and cortical area 17, were also present in the intermediate or caudal higher intensity transverse zones (Fig. 8). On the contrary, relatively lower signal ratios were marked in the M1, SII, and A1, which were present in the rostral or caudal higher intensity transverse zone in the cerebrum (Fig. 8).

The normalized signal ratio of T_2W-MRI intensity on each cortical area was shown in Fig. 8. Two-way ANOVA revealed a significant effect on cortical areas ($F_{5,108} = 7.400, P < 0.001$), but not on sexes or interactions between cortical areas and sexes (Fig. 8). Interestingly, the short TR/TE-MRI signal ratio had a close negative correlation with the density of MBP immunoreactive fibers (males, $r = -0.440$; females, $r = -0.481$), but the T_2W-MRI signal ratio did not (males, $r = 0.013$; females, $r = -0.025$) (Fig. 9). Thus, the signal intensity of short TR/TE-MRI in the cerebral cortex reflected the myelin density, and the MIP color maps of short TR/TE-MRI could reproduce the myeloarchitecture of the cerebral cortex in 3D.

Discussion

Ex vivo MRI using the fixed brain provides detailed morphology of the brain greater than that of *in vivo* MRI (Benveniste and Blackband, 2006). Several previous studies have characterized the cerebral morphology of adult ferret at various postnatal stages using MRI such as T_2-weighted MRI and DTI *in vivo* (Barnette et al., 2009; Kroenke et al., 2009; Neal et al., 2006). The present study further characterized the detailed morphology of the ferret cerebrum and its sexual dimorphism using MRI-based morphometry. Ferrets have advantages as an experimental model for studying the plasticity and development of the central nervous system. In particular, the ferret's cerebral cortical morphology matures in a regular sequence of sulcation and gyration during the first 2 postnatal weeks (Sawada and Watanabe, 2012), with a trajectory similar to that of the gyrification processes of the cerebrum of humans and non-human primates (Sawada et al., 2012). Also, the massive expansion of oSVZ with Pax6-expressing basal radial glia, which is thought to be correlated with the evolution and gyrification of the cerebral cortex (Hevner and Haydar, 2012), was confirmed during early postnatal ages (Fietz et al., 2010; Martínez-Cerdeño et al., 2012). Because experimental magnifications such as drug administration and stress loading are applied directly to the pups, the ferret is an advantageous model for studying human developmental and psychological disorders with gyrification abnormalities, i.e., schizophrenia and autism (Bonnici et al., 2007; Harden et al., 2004; Harris et al., 2004a,b; Jou et al., 2005; Kippenhan et al., 2005; Kulynych et al., 1997; Levitt et al., 2003; Nierenberg et al., 2005; Rapoport et al., 2005; Sallet et al., 2003; Vogeley et al., 2001). The present study provides MRI reference for the cerebral morphology of male and female ferrets.

In our previous study (Sawada and Watanabe, 2012), the enhanced leftward asymmetry of the cortical convolution in the visual cortex of males was observed as a sex-related morphological change in the ferret cerebrum. In the present study, sexual dimorphism of the ferret cerebrum was characterized by region-specific reductions in the volumes of the cortex and subcortical white matter found in females than in males, and by region-nonspecific changes in physiochemical properties of the cortex reflected by short TR/TE-MRI. Several studies have conducted quantitative analyses of the sexual dimorphism of cerebral morphology, such as the greater rightward bias in men than in women in the cortical volumes across all cerebral lobes except for the parietal lobe (Carne et al., 2006); overall greater thickness of the cerebral cortex in men than in women (Sowell et al., 2007); and right-dominant cortical thickness in male but not female rats (Diamond, 1987; Diamond, 1991; Stewart and Kolb, 1988). In other cerebral regions, sexual dimorphism was detected in volumes of the hippocampus, caudate nucleus and globus pallidus in humans (Giedd et al., 1997; Suzuki et al., 2005), and in the hippocampus and olfactory bulb in mice (Koshibu et al., 2004; Spring et al., 2007). A larger volume of amygdala in males than in females was marked in mice (Koshibu et al., 2004), but not in humans (Kim et al., 2012) and rhesus monkeys (Franklin et al., 2000). Although a larger volume of human amygdala in men than women was reported (Giedd et al., 1997; Goldstein et al., 2001), such a difference is considered to depend on age rather than sex (Kim et al., 2012). Therefore, sexual dimorphism of the volumes of each cerebral region differs among mammalian species. Since sex-related volume changes in left and/or right side(s) of particular regions of the cerebral cortex, amygdala and hippocampus are involved in schizophrenia (Exner et al., 2008), amnestic mild cognitive impairment, Alzheimer's disease (Skup et al., 2011), and panic disorder (Asami et al., 2009) in humans, the volumes of various cerebral regions in male and female ferrets in the present study may provide useful information for investigating neurodevelopmental and psychological disorders exhibiting sex-related prevalence.

In the present study, detailed laminar cytoarchitecture of the olfactory bulb could be reproduced by short TR/TE-MRI. In a previous study by Boretius et al. (2009), the mitral cell layer of the olfactory had been distinguished as having a low signal intensity by optimized T_2-weighted fast spin-echo MRI at 9.4 T with high resolution ($40 \times 40 \times 300$ μm). Their study further delineated cell layers of cerebral cortex, hippocampus and cerebellum. However, our procedure in T_2W-MRI measurements (7-T; resolution = $150 \times 150 \times 2000$ μm) failed to delineate the cell layers of the olfactory bulb as well as the cerebral cortex and hippocampus. Further study will be needed to establish optimal procedures of T_2W-MRI measurements for delineation of cell layers in various brain regions in ferret *ex vivo*.

In a previous study using common marmosets, T_1-weighted MRI represented myeloarchitecture in the cerebral cortex (Bock et al., 2009). The present study reveals a negative correlation of short TR/TE-MRI with the density of MBP-immunoreactive fibers in the ferret cerebral cortex. In the present study, reduced short TR/TE-MRI intensity may be related to short tissue T_1 in myelinated fibers, which is strongly influenced by a signal reduction due to T_2 shortening in the short TR/TE of high-field MRI. The cerebral cortex has natural topographic parturition defined by chemoarchitectonic staining. For example, immunostaining for non-phosphorylated forms of the neurofilament heavy chain (NFH; recognized by anti-SMI-32) and myelin staining define the regional architectural parcellation of the cortex, which is relevant to the cortical areas (Boire et al., 2005; Cruz-Rizzolo et al., 2011; Mellott et al., 2010; Van De Werd et al., 2010; van der Gucht et al., 2007). Such a chemical parcellation has been well characterized in the visual and posterior parietal cortices in ferrets (Homman-Ludiye et al., 2010; Innocenti et al., 2002; Manger et al., 2004). In the present study, short TR/TE-MRI-based MIP color maps revealed an array of higher and lower short TR/TE-MRI intensity transverse zones throughout the ferret cerebral cortex, which was reminiscent of the functional cortical areas. Therefore, the functional cortical areas relevant to myelin fiber density may be reproduced in 3D by short TR/TE-MRI-based MIP color maps.

In some gyrencephalic animals including humans, cerebral sulci are used as reproducible landmarks for delineating the cortical areas on MRI (Maudgil et al., 1998; Zilles et al., 1997). However, it is difficult to define the functional cortical areas of lissencephalic animals by non-invasive *in vivo* imaging techniques such as MRI and CT. Therefore, short TR/TE-MRI-based MIP color maps of the cerebral cortex may be useful for investigating the organization of the functional cortical areas and their abnormalities, particularly in lissencephalic animals such as rats and mice.

Normalized signal ratios of short TR/TE- and T_2W-MRI differ among tissues, and are useful for the diagnosis of injuries, diseases and developmental disorders of the brain. In the present study, an overall decrease was found in the signal ratios of short TR/TE-MRI of

the cerebral cortex and the major subcortical and archicortical structures. It is known that both shortening of T_1 and T_2 are altered by various physiochemical properties in tissues such as water diffusion (Holland et al., 1986) and magnetization transfer (Ogg and Steen, 1988). Myelination is known as one of the factors that alters the signal ratios of T_1-weighted and T_2-weighted MRIs in brain tissue (Holland et al., 1986). However, semi-quantitative immunohistochemical evaluation in the present study revealed no sex differences in myelin fiber density throughout the cerebral cortex, while the density was varied among functional cortical areas. It remains unclear why the signal ratio of short TR/TE-MRI was higher in males than in females in the present study. Other factors altering short TR/TE- and T_2W-MRI signals such as water contents of extracellular matrix and cell density (Prayer et al., 2006) may differ between sexes in the ferret cerebral tissues.

In conclusion, the present study is, to our knowledge, the first to characterize the detailed cerebral morphology of young adult ferrets and to describe its sexual dimorphism by two approaches using high-field MRI and MRI-based morphometry. As a further consideration, sexual dimorphism of the shapes and positions of each cerebral structure should be characterized in ferrets. However, since our brain samples were removed from skulls before MRI measurements, some artifact changes such as slight shrinkage of the brain tissues and reduced volume of ventricle (Ma et al., 2008) may hinder obtaining exact data regarding the shape and positions of cerebral structures. *In vivo* studies will also be needed. On the other hand, the present study provides full 3D brain coverage of MRI references for normal cerebral morphology of ferrets to investigate pathogenesis of sex-related neurodevelopmental and psychological disorders, i.e., autism (Levitt et al., 2003; Harden et al., 2004), schizophrenia (Exner et al., 2008), amnestic mild cognitive impairment, Alzheimer's disease (Skup et al., 2011), and panic disorder (Asami et al., 2009). Furthermore, short TR/TE-MRI-based MIP could visualize functional cortical areas related to myeloarchitecture in 3D. Such an approach makes it possible to investigate the functional organization of the cerebral cortex and its abnormalities, using MRI in a conventional manner.

Supplementary data to this article can be found online at http://dx.doi.org/10.1016/j.neuroimage.2013.06.024.

Acknowledgments

This study was supported by JSPS KAKENHI (23590223), and partly supported by "Funding Program for World-Leading Innovative R&D on Science and Technology (FIRST Program)" for MRI devices. The authors wish to thank Mr. Nobuhiro Nitta (Molecular Imaging Center, National Institute of Radiological Sciences, Chiba, Japan) for MRI measurements, and Ms. Misaki Watanabe (The Department of Nursing, Faculty of Medical and Health Sciences, Tsukuba International University, Tsuchiura, Ibaraki, Japan) for her generous assistance.

Conflict of interest

There are no conflicts of interest.

References

Asami, T., Yamasue, H., Hayano, F., Nakamura, M., Uehara, K., Otsuka, T., Roppongi, T., Nihashi, N., Inoue, T., Hirayasu, Y., 2009. Sexually dimorphic gray matter volume reduction in patients with panic disorder. Psychiatry Res. 173, 128–134.

Barnette, A.R., Neil, J.J., Kroenke, C.D., Griffith, J.L., Epstein, A.A., Bayly, P.V., Knutsen, A.K., Inder, T.E., 2009. Characterization of brain development in the ferret via MRI. Pediatr. Res. 66, 80–84.

Benveniste, H., Blackband, S.J., 2006. Translational neuroscience and magnetic-resonance microscopy. Lancet Neurol. 5, 536–544.

Bock, N.A., Kocharyan, A., Liu, J.V., Silva, A.C., 2009. Visualizing the entire cortical myelination pattern in marmosets with magnetic resonance imaging. J. Neurosci. Methods 185, 15–22.

Boire, D., Desgent, S., Matteau, I., Ptito, M., 2005. Regional analysis of neurofilament protein immunoreactivity in the hamster's cortex. J. Chem. Neuroanat. 29, 193–208.

Bonnici, H.M., William, T., Moorhead, J., Stanfield, A.C., Harris, J.M., Owens, D.G., Johnstone, E.C., Lawrie, S.M., 2007. Pre-frontal lobe gyrification index in schizophrenia, mental retardation and comorbid groups: an automated study. Neuroimage 35, 648–654.

Boretius, S., Kasper, L., Tammer, R., Michaelis, T., Frahm, J., 2009. MRI of cellular layer in mouse brain *in vitro*. Neuroimage 47, 1252–1260.

Carne, R.P., Vogrin, S., Litewka, L., Cook, M.J., 2006. Cerebral cortex: an MRI-based study of volume and variance with age and sex. J. Clin. Neurosci. 13, 60–72.

Clancy, B., Darlington, R.B., Finlay, B.L., 2001. Translating time across mammalian species. Neuroscience 105, 7–17.

Cruz-Rizzolo, R.J., De Lima, M.A., Ervolino, E., de Oliveira, J.A., Casatti, C.A., 2011. Cyto-, myelo- and chemoarchitecture of the prefrontal cortex of the *Cebus* monkey. BMC Neurosci. 12, 6. http://dx.doi.org/10.1186/1471-2202-12-6.

Diamond, M.C., 1987. Sex differences in the rat forebrain. Brain Res. 434, 235–240.

Diamond, M.C., 1991. Hormonal effects on the development or cerebral lateralization. Psychoneuroendocrinology 16, 121–129.

Exner, C., Nehrkorn, B., Martin, V., Huber, M., Shiratori, K., Rief, W., 2008. Sex-dependent hippocampal volume reductions in schizophrenia relate to episodic memory deficits. J. Neuropsychiatry Clin. Neurosci. 20, 227–230.

Fietz, S.A., Kelava, I., Vogt, J., Wilsch-Bräuninger, M., Stenzel, D., Fish, J.L., Corbeil, D., Riehn, A., Distler, W., Nitsch, R., Huttner, W.B., 2010. OSVZ progenitors of human and ferret neocortex are epithelial-like and expand by integrin signaling. Nat. Neurosci. 13, 690–699.

Foxworthy, W.A., Meredith, M.A., 2011. An examination of somatosensory area SIII in ferret cortex. Somatosens. Mot. Res. 28, 1–10.

Giedd, J.N., Castellanos, F.X., Rajapakse, J.C., Vaituzis, A.C., Rapoport, J.L., 1997. Sexual dimorphism of the developing human brain. Prog. Neuropsychopharmacol. Biol. Psychiatry 21, 1185–1201.

Goldstein, J.M., Seidman, L.J., Makris, N., Ahern, T., O'Brien, L.M., Caviness Jr., V.S., Kennedy, D.N., Faraone, S.V., Tsuang, M.T., 2001. Normal sexual dimorphism of the adult human brain assessed by *in vivo* magnetic resonance imaging. Cereb. Cortex 11, 490–497.

Harden, A.Y., Jou, R.J., Keshavan, M.S., Varma, R., Minshew, N.J., 2004. Increased frontal cortical folding in autism: a preliminary MRI study. Psychiatry Res. 131, 263–268.

Harris, J.M., Yates, S., Miller, P., Best, J.J.K., Johnstone, E.C., Lawrie, S.M., 2004a. Gyrification in first-episode schizophrenia: a morphometric study. Biol. Psychiatry 55, 141–147.

Harris, J.M., Whalley, H., Yates, S., Miller, P., Johnstone, E.C., Lawrie, S.M., 2004b. Abnormal cortical folding in high-risk individuals: a predictor for the development of schizophrenia? Biol Psychiatry 56, 182–189.

Hevner, R.F., Haydar, T.F., 2012. The (not necessarily) convoluted role of basal radial glia in cortical neurogenesis. Cereb. Cortex 22, 465–468.

Holland, B.A., Haas, D.K., Norman, D., Brant-Zawadzki, M., Newton, T.H., 1986. MRI of normal brain maturation. Am. J. Neuroradiol. 7, 201–208.

Homman-Ludiye, J., Manger, P.R., Bourne, J.A., 2010. Immunohistochemical parcellation of the ferret (*Mustela putorius*) visual cortex reveals substantial homology with the cat (*Felis catus*). J. Comp. Neurol. 518, 4439–4462.

Innocenti, G.M., Manger, P.R., Masiello, I., Colon, I., Tetton, L., 2002. Architecture and callosal connections of visual areas 17, 18, 19 and 21 in the ferret (*Mustela putoris*). Cereb. Cortex 12, 411–422.

Jou, R.J., Hardan, A.Y., Keshavan, M.S., 2005. Reduced cortical folding in individuals at high risk for schizophrenia: a pilot study. Schizophr. Res. 75, 309–313.

Keniston, L.P., Allman, B.L., Meredith, M.A., Clemo, H.R., 2009. Somatosensory and multisensory properties of the medial bank of the ferret rostral suprasylvian sulcus. Exp. Brain Res. 196, 239–251.

Kim, H.J., Kim, N., Kim, S., Hong, S., Park, K., Lim, S., Park, J.M., Na, B., Chae, Y., Lee, J., Yeo, S., Choe, I.H., Cho, S.Y., Cho, G., 2012. Sex differences in amygdala subregions: evidence from subregional shape analysis. Neuroimage 60, 2054–2661.

Kippenhan, J.S., Olsen, R.K., Mervis, C.B., Morris, C.A., Kohn, P., Meyer-Lindenberg, A., Berman, K.F., 2005. Genetic contributions to human gyrification: sulcal morphometry in Williams syndrome. J. Neurosci. 25, 7840–7846.

Koshibu, K., Levitt, P., Ahrens, E.T., 2004. Sex-specific, postpuberty changes in mouse brain structures revealed by three-dimensional magnetic resonance microscopy. Neuroimage 22, 1636–1645.

Koyanagi, Y., Sawada, K., Sakata-Haga, H., Jeong, Y.G., Fukui, Y., 2006. Increased serotonergic innervation of lumbosacral motoneurons of rolling mouse Nagoya in correlation with abnormal hindlimb extension. Anat. Histol. Embryol. 35, 387–392.

Kroenke, C.D., Taber, E.N., Leigland, L.A., Knutsen, A.K., Bayly, P.V., 2009. Regional patterns of cerebral cortical differentiation determined by diffusion tensor MRI. Cereb. Cortex 19, 2916–2929.

Kulynych, J.J., Luevano, L.F., Jones, D.W., Weinberger, D.R., 1997. Cortical abnormality in schizophrenia: an *in vivo* application of the gyrification index. Biol. Psychiatry 41, 995–999.

Lawes, I.N.C., Andrews, P.L.R., 1998. Neuroanatomy of the ferret brain, In: Fox (Ed.), Biology and Diseases of the Ferret, 2nd ed. Lippincott Williams and Wilkins, pp. 71–102.

Levitt, J.G., Blanton, R.E., Smalley, S., Thompson, P.M., Guthrie, D., McCracken, J.T., Sadoun, T., Heinichen, L., Toga, A.W., 2003. Cortical sulcal maps in autism. Cereb. Cortex 13, 728–735.

Ma, Y., Smith, D., Hof, P.R., Foerster, B., Hamilton, S., Blackband, S.J., Yu, M., Benveniste, H., 2008. *In vivo* 3D digital atlas database of the adult C57BL/6J mouse brain by magnetic resonance microscopy. Front. Neuroanat. 2, 1. http://dx.doi.org/10.3389/neuro.05.001.2008.

Maher, J.A., DeStefano, J., 2004. The ferret: an animal model to study influenza virus. Lab. Anim. 33, 50–53.

Manger, P.R., Nakamura, H., Valentiniene, S., Innocenti, G.M., 2004. Visual areas in the lateral temporal cortex of the ferret (*Mustela putorius*). Cereb. Cortex 14, 676–689.

Martínez-Cerdeño, V., Cunningham, C.L., Camacho, J., Antczak, J.L., Prakash, A.N., Cziep, M.E., Walker, A.I., Noctor, S.C., 2012. Comparative analysis of the subventricular zone in rat, ferret and macaque: evidence for an outer subventricular zone in rodents. PLoS One 7, e30178.

Maudgil, D.D., Free, S.L., Sisodiya, S.M., Lemieux, L., Woermann, F.G., Fish, D.R., Shorvon, S.D., 1998. Identifying homologous anatomical landmarks on reconstructed magnetic resonance images of the human cerebral cortical surface. J. Anat. 193, 559–571.

Mellott, J.G., Van der Gucht, E., Lee, C.C., Carrasco, A., Winer, J.A., Lomber, S.G., 2010. Areas of cat auditory cortex as defined by neurofilament proteins expressing SMI-32. Hear. Res. 267, 119–136.

Neal, J., Takahashi, M., Silva, M., Tiao, G., Walsh, C.A., Sheen, V.L., 2006. Insights into the gyrification of developing ferret brain by magnetic resonance imaging. J. Anat. 210, 66–77.

Nierenberg, J., Salisbury, D.F., Levitt, J.J., David, E.A., McCarley, R.W., Shenton, M.E., 2005. Reduced left angular gyrus volume in first-episode schizophrenia. Am. J. Psychiatry 162, 1539–1541.

Ogg, R.J., Steen, R.G., 1988. Age-related changes in brain T_1 are correlated with iron concentration. Magn. Reson. Med. 40, 749–753.

Poluch, S., Jablonska, B., Juliano, S.I., 2008. Alteration of interneuron migrationin a ferret model of cortical dysplasia. Cereb. Cortex 18, 78–92.

Prayer, D., Kasprian, G., Krampl, E., Ulm, B., Witzani, L., Prayer, L., Brugger, P.C., 2006. MRI of normal fetal brain development. Eur. J. Radiol. 57, 199–216.

Rapoport, J.L., Addington, A., Frangou, S., 2005. The neurodevelopmental model of schizophrenia: what can very early onset cases tell us? Curr. Psychiatry Rep. 7, 81–82.

Sallet, P.C., Elkis, H., Alves, T.M., Oliveira, J.R., Sassi, E., Campi de Castro, C., Busatto, G.F., Gattaz, W.F., 2003. Reduced cortical folding in schizophrenia: an MRI morphometric study. Am. J. Psychiatry 160, 1606–1613.

Sawada, K., Watanabe, M., 2012. Development of cerebral sulci and gyri in ferrets (*Mustela putorius*). Congenit. Anom. (Kyoto) 52, 168–175.

Sawada, K., Fukunishi, K., Kashima, M., Saito, S., Sakata-Haga, H., Aoki, I., Fukui, Y., 2012. Fetal gyrification in cynomolgus monkeys: a concept of developmental stages of gyrification. Anat. Rec. (Hoboken) 295, 1065–1074.

Schlaepfer, T.E., Harris, G.J., Tien, A.Y., Peng, L., Lee, S., Pearlson, G.D., 1995. Structural differences in the cerebral cortex of healthy female and male subjects: a magnetic resonance imaging study. Psychiatry Res. 11, 129–135.

Sheehan, D.C., Hrapchak, B.B., 1980. Theory and Practice of Histotechnology, 2nd ed. Battelle Press, Columbus/Richland.

Skup, M., Zhu, H., Wang, Y., Giovanello, K.S., Lin, J.A., Shen, D., Shi, F., Gao, W., Lin, W., Fan, Y., Zhang, H., 2011. Sex differences in grey matter atrophy patterns among AD and aMCI patients: results from ADNI. Neuroimage 56, 890–906.

Smart, I.H., McSherry, G.M., 1986. Gyrus formation in the cerebral cortex in the ferret. I. Description of the external histological changes. J. Anat. 146, 141–152.

Sowell, E.R., Peterson, B.S., Kan, E., Woods, R.P., Yoshii, J., Bansal, R., Xu, D., Zhu, H., Thompson, P.M., Toga, A.W., 2007. Sex differences in cortical thickness mapped in 176 healthy individuals between 7 and 87 years of age. Cereb Cortex 17, 1550–1560.

Spring, S., Lerch, J.P., Henkelman, R.M., 2007. Sexual dimorphism revealed in the structure of the mouse brain using three-dimensional magnetic resonance imaging. Neuroimage 35, 1424–1433.

Stewart, J., Kolb, B., 1988. The effects of neonatal gonadectomy and prenatal stress on cortical thickness and asymmetry in rats. Behav. Neural Biol. 49, 344–360.

Suzuki, M., Hagino, H., Nohara, S., Zhou, S.Y., Kawasaki, Y., Takahashi, T., Matsui, M., Seto, H., Ono, T., Kurachi, M., 2005. Male-specific volume expansion of the human hippocampus during adolescence. Cereb. Cortex 15, 187–193.

Tao, J.D., Barnette, A.R., Griffith, J.L., Neil, J.J., Inder, T.E., 2012. Histopathologic correlation with diffusion tensor imaging after chronic hypoxia in the immature ferret. Pediatr. Res. 71, 192–198.

Van de Werd, H.J., Rajkowska, G., Evers, P., Uylings, H.B., 2010. Cytoarchitectonic and chemoarchitectonic characterization of the prefrontal cortical areas in the mouse. Brain Struct. Funct. 214, 339–353.

Van der Gucht, E., Hof, P.R., Van Brussel, L., Burnat, K., Arckens, L., 2007. Neurofilament protein and neuronal activity markers define regional architectonic parcellation in the mouse visual cortex. Cereb. Cortex 17, 2805–2819.

Vogeley, K., Tepest, R., Pfeiffer, U., Schneider-Axmann, T., Maier, W., Honer, W.G., Falkai, P., 2001. Right frontal hypergyria differentiation in affected and unaffected siblings from families multiply affected with schizophrenia: a morphometric MRI study. Am. J. Psychiatry 158, 494–496.

Wright, I.C., McGuire, P.K., Poline, J.B., Travere, J.M., Murray, R.M., Frith, C.D., Frackowiak, R.S., Friston, K.J., 1995. A voxel-based method for the statistical analysis of gray and white matter density applied to schizophrenia. Neuroimage 2, 244–252.

Zilles, K., Schleicher, A., Langemann, C., Amunts, K., Morosan, P., Palomero-Gallagher, N., Schormann, T., Mohlberg, H., Bürgel, U., Steinmetz, H., Schlaug, G., Roland, P.E., 1997. Quantitative analysis of sulci in the human cerebral cortex: development, regional heterogeneity, gender difference, asymmetry, intersubject variability and cortical architecture. Hum. Brain Mapp. 5, 218–221.